FAIRCHILD
SPACE

FSC-ESD-217-93-519A

RADIOISOTOPE THERMOPHOTOVOLTAIC (RTPV) GENERATOR AND ITS APPLICABILITY TO AN ILLUSTRATIVE SPACE MISSION

A. Schock
M. Mukunda
T. Or
V. Kumar
G. Summers

Fairchild Space and Defense Corporation
Germantown, MD 20874

February 14, 1994

Abstract

The paper describes the results of a DOE-sponsored design study of a radioisotope thermophotovoltaic generator (RTPV), to complement similar studies of Radioisotope Thermoelectric Generators (RTGs) and Stirling Generators (RSGs) previously published by the author. Instead of conducting a generic study, it was decided to focus the design effort by directing it at a specific illustrative space mission, Pluto Fast Flyby (PFF). That mission, under study by JPL, envisages a direct eight-year flight to Pluto (the only unexplored planet in the solar system), followed by comprehensive mapping, surface composition, and atmospheric structure measurements during a brief flyby of the planet and its moon Charon, and transmission of the recorded science data to Earth during a post-encounter cruise lasting up to one year.

Because of Pluto's long distance from the sun (30-50 A.U.) and the mission's large energy demand, JPL has baselined the use of a radioisotope power system for the PFF spacecraft. RTGs have been tentatively selected, because they have been successfully flown on many space missions, and have demonstrated exceptional reliability and durability. The only reason for exploring the applicability of the far less mature RTPV systems is their potential for much higher conversion efficiencies, which would greatly reduce the mass, and cost of the required radioisotope heat source. Those attributes are particularly important for the PFF mission, which - like all NASA missions under current consideration - is severely mass- and cost-limited.

The paper describes the design of an RTPV system consisting of a radioisotope heat source, a thermophotovoltaic converter, and an optimized heat rejection system; and depicts its integration with the PFF spacecraft. It then describes the thermal, electrical, and structural analysis which led to that optimized design, and compares the computed performance of an RTPV system to that of an RTG designed for the same mission. Our analytical results indicated that - when fully developed - it could result in a 60% reduction of the heat source's mass, cost, and fuel loading, a 50% reduction of generator mass, a tripling of the power system's specific power, and a quadrupling of its efficiency.

The paper concludes by briefly summarizing the RTPV's current technology status and assessing its potential applicability for the PFF mission. For other power systems (e.g. RTGs), demonstrating their flight readiness for a long-term mission is a very time-consuming process. But for the case of the described RTPV design, the paper lists a number of factors, primarily its cold (0 to 10°C) converter temperature, that may greatly reduce the need for long-term tests to demonstrate generator lifetime. In any event, our analytical results suggest that the RTPV generator, when developed by DOE and/or NASA, would be quite valuable not only for the Pluto mission but also for other future missions requiring small, long-lived, low-mass generators.

INTRODUCTION

Major changes are occurring in the field of space technology. For budgetary and other reasons, there is a strong drive for cheaper and quicker space science missions, partly through use of smaller and lighter spacecraft and their components. Among those components is the power system, which typically represents a major fraction of the cost and mass of the spacecraft.

For powering small, long-duration spacecraft, there are two types of power sources: solar and nuclear (specifically radioisotope systems, since nuclear reactors are too large and massive for small spacecraft). Whenever they have a choice, mission designers prefer solar power systems, because of their lower cost and simpler launch approval process. But they don't always have a choice, because there are applications which may be too far from the sun or at high planetary latitudes or dust-obstructed locations with too little sunlight for effective solar power generation. For those applications, radioisotope power sources may be most attractive or even enabling (e.g., Apollo, Pioneer 10/11, Voyager, Viking, Galileo, Ulysses, Cassini).

But present radioisotope thermoelectric generators (RTGs) are quite costly, because of the high cost of radioisotope heat sources and the low efficiency (~7%) of thermoelectric conversion systems. To reduce the cost of radioisotope power systems, it is necessary to achieve major increases in conversion efficiencies in order to diminish the number of costly heat source modules needed for a given application. Fortunately, there are a number of advanced conversion systems that may be able to triple the conversion efficiency of present thermoelectric converters. These include the Stirling [1], AMTEC [2], and the thermophotovoltaic (TPV) [3] options. The latter is the basis of the design study described in the present paper.

The TPV concept is an outgrowth of progress on photovoltaic (PV) solar cells. In solar systems, the photovoltaic cells convert solar radiation into electricity, while in TPV systems they convert infrared radiation emitted by a hot surface. If the hot surface is heated by a radioisotope heat source, the resultant system is referred to as a radioisotope thermophotovoltaic (RTPV) generator. This concept had been recognized for some time, but until recently the available materials did not permit competitive efficiencies.

Since the infrared spectrum at reasonable temperatures peak at a very different wavelength than the solar spectrum, TPV systems require photovoltaic cells with significantly different band gap energies. Conventional PV materials, like silicon or gallium arsenide (GaAs), would be quite inefficient in TPV devices. But gallium antimonide (GaSb) or gallium-indium antimonide have spectral properties that make them attractive candidates for TPV applications. This was recognized by Boeing personnel, who had been investigating GaSb cells in back of conventional GaAs cells, to produce a tandem solar cell which in their experiments yielded efficiencies up to 35%, significantly higher than plain GaAs cells [4]. The high efficiencies of the tandem cells derive from the spectral characteristics of GaSb, which enable it to utilize the wavelengths that pass through the GaAs cells. These same characteristics make GaSb attractive for TPV applications.

Boeing personnel also recognized that the efficiency of the TPV system could be greatly improved by interposing a spectrally selective filter between the hot surface and the GaSb cell. The filter is designed to transmit those wavelengths that can be efficiently converted to electricity by GaSb, and to reflect other wavelengths back to the heat source, to conserve energy. It is the filter that makes possible the high efficiencies currently projected for TPV systems.

The present paper deals with the design and thermal, electrical, and structural analyses of an integrated system consisting of a radioisotope heat source, an array of TPV converter cells, and an optimized radiator for rejecting the waste heat to space. As will be seen, the integrated RTPV system - when successfully developed - has attributes that would make it an excellent candidate as a lighter and cheaper replacement for present RTGs. Thus, it could be applied to a number of potential missions. But to focus the present design study, it was decided to design an RTPV generator for a specific application, the Pluto Fast Flyby (PFF) mission, which is an excellent example of the trend towards smaller, lighter, and cheaper spacecraft and subsystems [5].

Pluto is the only unexplored planet in the solar system, and there is great scientific interest in a spacecraft reconnaissance of the planet and its large moon Charon, before the atmosphere of Pluto condenses as it recedes from the sun [6]. As its name implies, the Pluto Fast Flyby mission under study by JPL for NASA contemplates a spacecraft to "fly by" the planet rather than to orbit or land on it. This simplification permits major size, mass, and cost reductions, and greatly shortens the time for development of the spacecraft and for transit to Pluto. JPL is considering a launch around the year 2000, with two direct eight-year flights to Pluto (no gravity assist). The science data recorded during the brief Pluto flyby, including visual, infrared, ultraviolet, and radio observations of both sides of the planet/moon system, would then be transmitted to Earth during a post-encounter cruise lasting up to one year.

JPL's power demand schedule for the baseline PFF mission called for a peak (including 20% contingency) of 63 watts(e) at the end of the 9.2-year mission. At a distance of 30 or more astronomical units from the sun, the incident solar-flux is at least three orders of magnitude lower than at Earth, which would require very large solar arrays. In fact, it is unclear whether current solar arrays would function at Pluto at all, because of still unsolved Low-Intensity, Low-Temperature (LILT) effects on solar arrays. Therefore, JPL's baseline design called for the use of a radioisotope power source for PFF [7].

The spacecraft size reduction made possible by the flyby mission plan is illustrated in Figure 1, which compares the size of an early (1992) JPL baseline design with the much larger spacecraft of preceding RTG-powered interplanetary missions (Voyager, Galileo, Cassini). That PFF baseline design had an estimated mass (including propellant) of 165 kg, with a mass reduction goal to 112 kg. This implied a 47% mass reduction of the radioisotope power source, from 17.8 kg to 9.5 kg, clearly a very formidable goal.

Fig. 1 Comparative Size of PFF and Prior Spacecraft

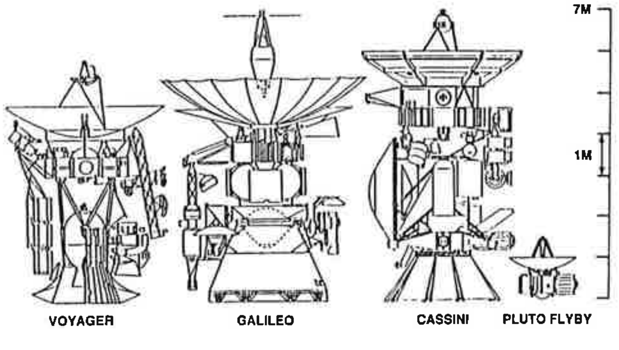

To support NASA and JPL, the Department of Energy's Radioisotope Power Systems Division commissioned Fairchild Space and Defense Corporation under Contract DE-AC01-93-32177 to prepare conceptual designs for a variety of PFF power source options, to help clarify the available options and to provide reliable mass estimates and technology status assessments. The study results are designed to support informed trade-off decisions by program management. Eight options were designed, analyzed, and reported on last year: five thermoelectric [8] and three Stirling systems [9]. None of these (except for a non-redundant Stirling system option) achieved the desired mass reduction goal. Since then, Fairchild has conducted a similar study, reported here, which shows that that goal can be achieved and substantially surpassed with an RTPV system. The report concludes with parametric performance summaries and their programmatic implications.

SYSTEM DESIGN

This section presents a description of the radioisotope heat source, the TPV converter, and the heat rejection radiator, and their system integration. Thermal, electrical, and structural analyses and optimization of the integrated system are presented in the subsequent section.

Radioisotope Heat Source

The radioisotope heat source for the RTPV design, like that for the RTG options analyzed in Fairchild's PFF study last year [8], are based on the General Purpose Heat Source (GPHS) modules [10]. These are the same modules that were used in the RTGs flown on the Galileo and Ulysses missions after very extensive safety analyses and tests and after passing stringent safety reviews, and that are slated for launch on the upcoming Cassini mission.

As shown in Figure 2, each GPHS module has a maximum thermal power of 250 watts, and contains four $^{238}PuO_2$ fuel pellets encapsulated in iridium-alloy clads designed to contain or immobilize the fuel in case of accidents before, during, and after launch. The remaining module components are graphitic and are designed to protect the integrity of the iridium clads. There are two impact shells and one aeroshell made of fine-weave pierced fabric (FWPF), a very tough high-temperature three-dimensional carbon-carbon composite.

The impact shells help to prevent breach of the clads during impact, and the aeroshell serves as an ablator in case of inadvertent atmospheric reentry. Between the impact shells and the aeroshell is a high-temperature thermal insulator consisting of a low-density composite of carbon-bonded carbon fibers (CBCF), to prevent overheating of the clads during the reentry heat pulse and overcooling and embrittlement of the clads during the subsequent subsonic atmospheric descent before earth impact.

For the present study, it was decided to base the RTPV generator design on the use of two GPHS modules, which is a 60% reduction from the five modules used in the RTG design for PFF [8].

Fig. 2 GPHS–General -Purpose Heat Source Module (250 Watts) Sectioned at Mid-Plane

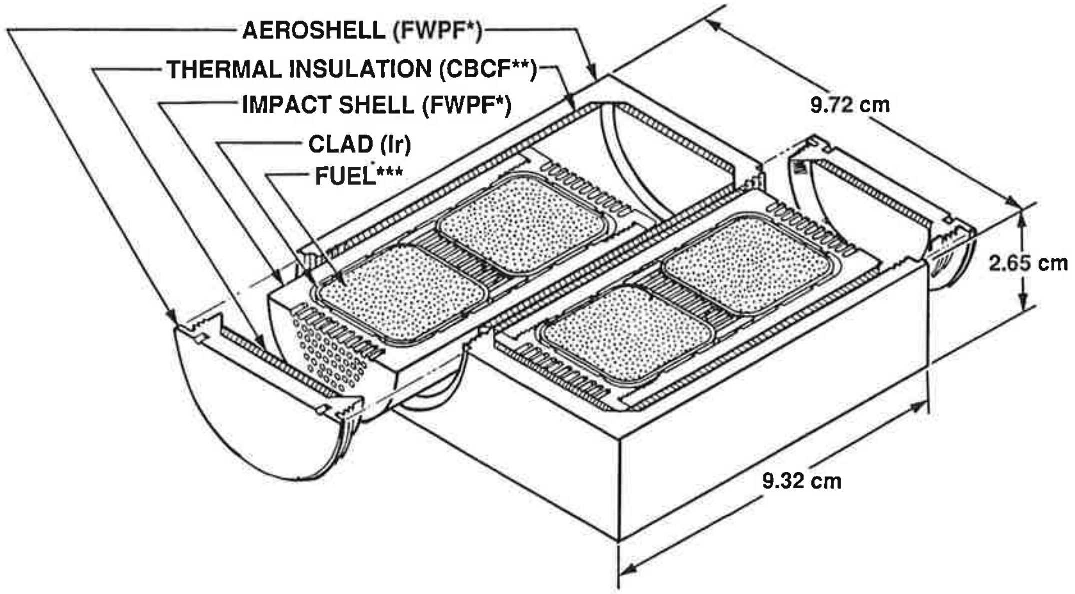

*Fine-Weave Pierced Fabric, a 90%-dense 3D carbon-carbon composite
**Carbon-Bonded Carbon Fibers, a 10%-dense high-temperature insulator
***62.5-watt ^{238} PuO_2 pellet

Thermophotovoltaic Converter Assembly

Figures 3 and 4 display horizontal and vertical cross-sections of the two-module heat source and of the photovoltaic converter, and Figure 5 shows an exploded trimetric view. As can be seen, the heat source's graphitic aeroshell is enclosed in an approximately cubical molybdenum canister. The inside of the canister's end caps is lined with iridium to prevent contact between the graphite and molybdenum. The outside of the canister's side walls is coated with tungsten to minimize sublimation, and also because tungsten has more favorable spectral emissivity characteristics than molybdenum. To reduce the temperatures in the heat source, the inside of the canister's side walls are roughened to raise their effective total emissivity to 0.60. So is the walls' outside, for reasons that will be explained in the Analysis Section.

Fig. 3 Horizontal Cross-Section of Converter
(Dimensions in Inches)

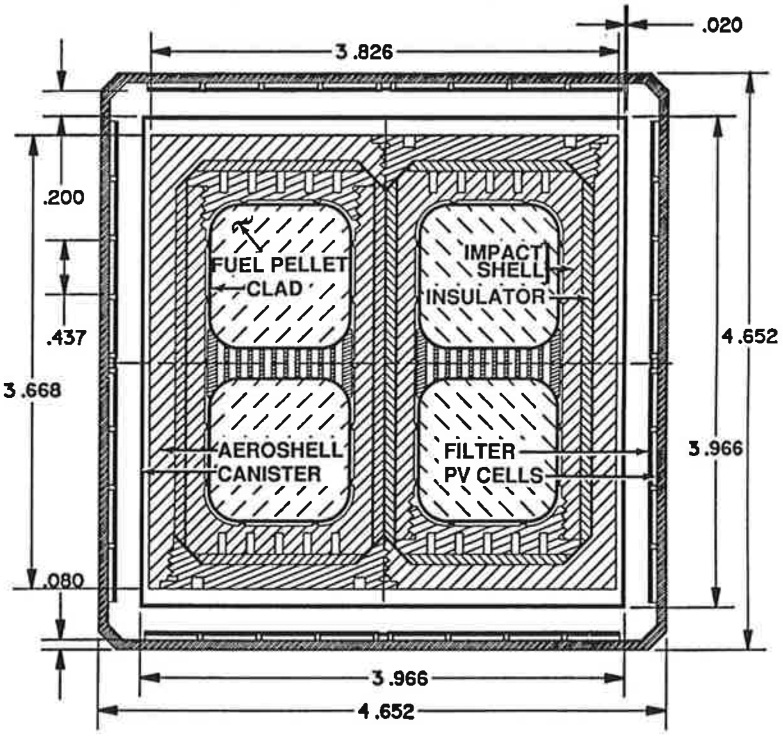

As indicated in Figure 3 and 4, each of the canister's four side faces radiates heat to a photovoltaic array of 8 x 8 gallium antimonide cells covered by a spectral filter. Each rectangular cell has dimensions of 0.428" x 0.437" (1.09 cm x 1.11 cm).

As seen in Figure 4, the canister has a vent tube to release the helium formed by alpha decay of the Pu-238 fuel to space. The vent tube terminates in a semi-permeable Viton seal, designed to maintain an internal pressure of a fraction of an atmosphere at the helium generation rate of 654 scc per year from the 500 watt(t) heat source. This pressure range is low enough to prevent excessive stress in the canister, but high enough to provide continuum conduction in the internal gas gaps, which greatly reduces the clad temperature. Reduced clad temperatures reduce grain growth and consequent embrittlement of the iridium alloy which is of critical importance in case of subsequent inadvertent Earth impact.

Fig. 4 Vertical Cross-Section of Converter

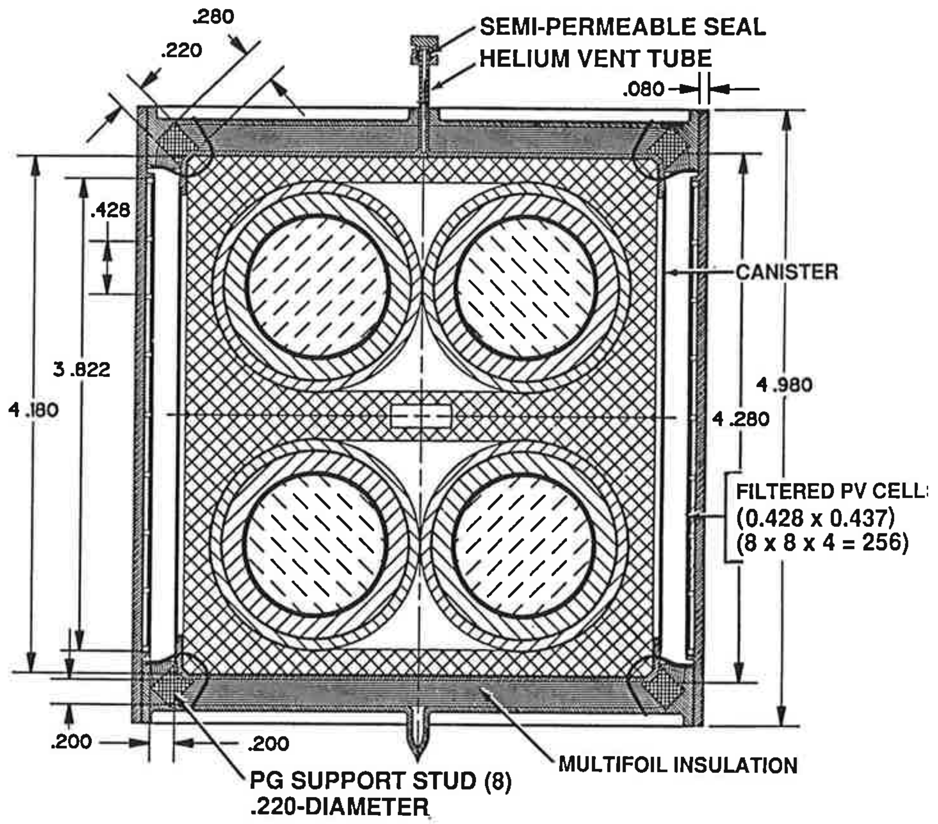

Since the heat source modules are contained in a monolithic canister, unlike the stack of unsupported modules used in preceding RTGs [11], there is no need for a complex axial preload mechanism to hold the stack together during launch vibration. As indicated in Figure 4, each of the canister's eight corners is supported by a small cylindrical pyrolitic-graphite (PG) stud. PG has good compressive strength, and the axes of the eight cylindrical support studs all point at the center of the heat source. Thus, shear loads are minimized, and the canister is supported in every direction by compressive loads on the PG studs.

The thermal conductivity of PG is highly anisotropic, being two orders of magnitude lower in the c-direction than in the a-direction. The cylindrical studs are machined so that their axes lie in the c-direction to minimize thermal losses. For the dimensions shown, our analysis showed that only 3.6% of the heat source's thermal power is lost through the support studs.

As shown in Figure 4, the canister's two end faces are thermally insulated by a multifoil assembly, similar to those used in previous thermoelectric converters, and consisting of 60 layers of 0.0003" Mo foils separated by ZrO_2 spacer particles. Our analysis showed that only 2.2% of the thermal power is lost through the multifoil insulation. Thus, 94.2% of the generated heat is absorbed by the converter.

At each horizontal level, the cells are parallel-connected in groups of four, and these groups of parallel cells are series-connected in the converter's corners to groups in the next horizontal level. Thus, each generator side has two series-parallel networks of 8x4 cells, and the generator's eight networks are connected in series with each other. The series connectors are not shown but they could be formed by spot-welding projecting tabs located in the four empty housing corners shown in Figure 3. Figure 5 shows an exploded view of the converter and lists its construction materials.

Fig. 5 Exploded View of Converter

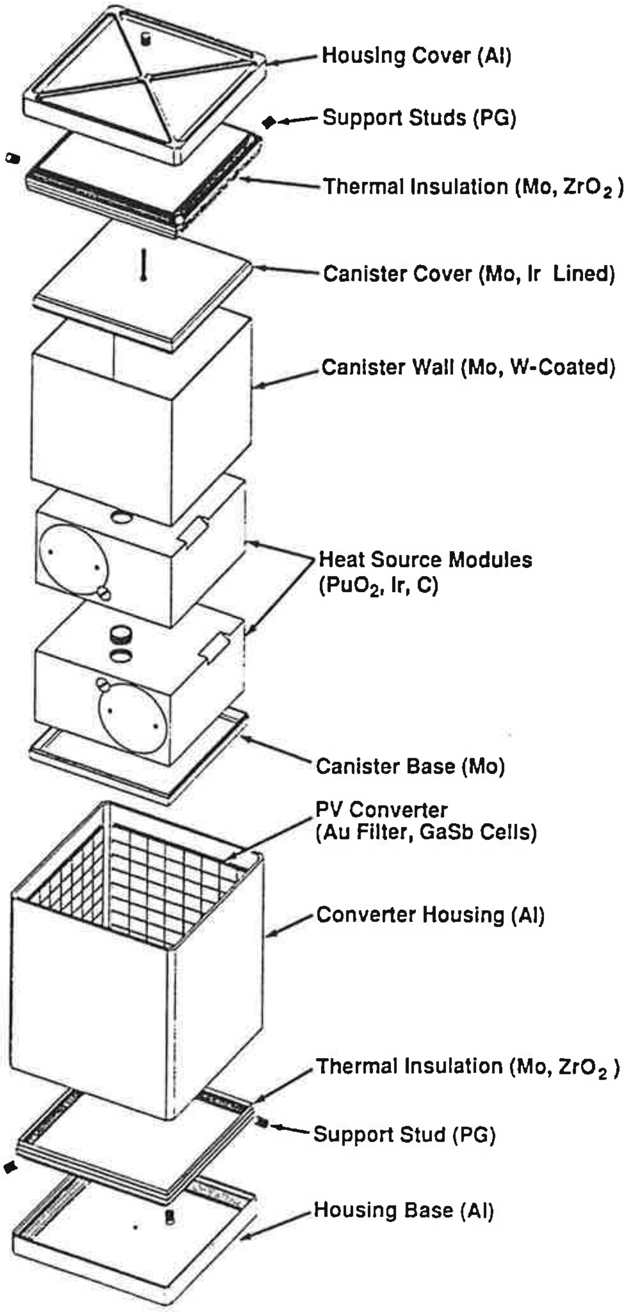

A schematic view of the cell interconnections is shown in Figure 6 for one generator side and in Figure 7 for all four sides. As seen, each side has terminals at its lower corners. At three corners of the generator the terminals of neighboring sides are connected together to form a 64x4 series-parallel network. At the fourth corner, leads from the two terminals are brought out of the generator housing through insulated feedthroughs for a total output of approximately 28 volts.

Fig. 6 Schematic View of Series-Parallel Network Connecting the 64 PV Cells on Each Converter Face

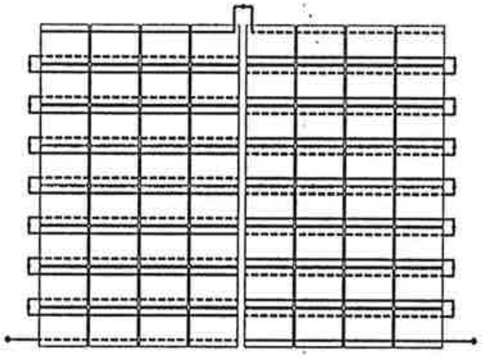

Fig. 7 Converter Network

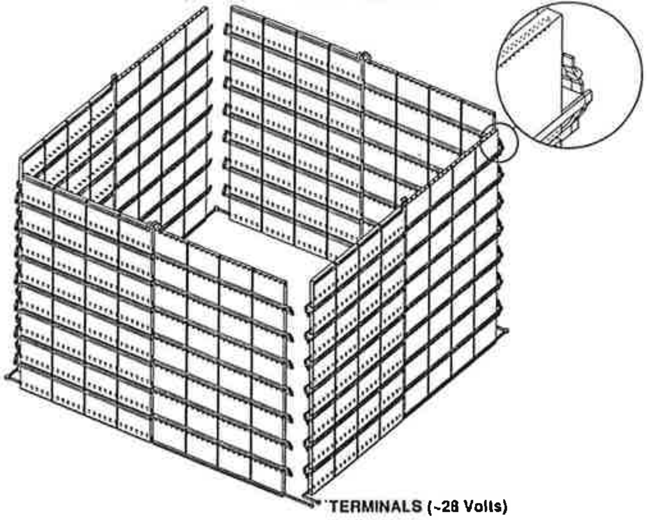

SYSTEM ANALYSIS

This section of the report describes the analysis which led to the optimized RTPV design depicted in the preceding section. It describes the thermal and electrical analyses of the TPV converter, the static and dynamic structural analyses of the long radiator fins, and the parametric analysis and optimization of the RTPV system. The concluding section compares the RTPV results to those of an RTG designed for the same mission and discusses their programmatic implications.

Thermal and Electrical Analysis of TPV Converter

This subsection presents a generic analysis of the thermophotovoltaic energy conversion process, not tied to any specific converter geometry or heat source thermal power. The equations derived will be applied to specific geometries in subsequent subsections.

The emitted heat flux in the wavelength interval λ to $\lambda + d\lambda$ from a black body at absolute temperature T is given by

$$q(\lambda)d\lambda = \frac{2\pi hc^2\lambda^{-5}d\lambda}{\exp(hc/\lambda kT)-1,} \tag{1}$$

where h and k are Planck's and Boltzmann's constants and c is the speed of light.

For a planar heat source S separated by a vacuum gap from a parallel planar converter C, the spectral energy flux leaving each surface is given by the sum of the emitted and reflected radiation:

$$q_s(\lambda)d\lambda = \varepsilon_s(\lambda)\frac{2\pi hc^2\lambda^{-5}d\lambda}{\exp(hc/\lambda kT_s)-1} + R_s(\lambda)q_c(\lambda)d\lambda, \tag{2}$$

$$q_c(\lambda)d\lambda = \varepsilon_c(\lambda)\frac{2\pi hc^2\lambda^{-5}d\lambda}{\exp(hc/\lambda kT_c)-1} + R_c(\lambda)q_s(\lambda)d\lambda, \tag{3}$$

where $\varepsilon(\lambda)$ and $R(\lambda)$ are the respective surface's spectral emissivity and reflectivity at wavelength λ.

The net radiative heat flux $q(\lambda)\ d\lambda$ emitted by the heat source and absorbed by the converter in the wavelength interval λ to $\lambda +\ d\lambda$ is given by

$$q(\lambda)\ d\lambda = [q_s(\lambda) - q_c(\lambda)]\ d\lambda. \tag{4}$$

Solving Eqs. (2) and (3) for $q_S(\lambda)$ and $q_C(\lambda)$ and inserting the results into Eq. (4), we obtain

$$q(\lambda)d\lambda = \frac{2\pi hc^2\lambda^{-5}}{1-R_s(\lambda)R_c(\lambda)}\left[\frac{\varepsilon_s(\lambda)[1-R_c(\lambda)]}{\exp(hc/\lambda kT_s)-1} - \frac{\varepsilon_c(\lambda)[1-R_s(\lambda)]}{\exp(hc/\lambda kT_c)-1}\right]d\lambda. \tag{5}$$

Since $T_C << T_S$ in the present case, the second term in the square bracket is negligible, and Eq. (5) reduces to

$$q(\lambda)d\lambda = \frac{2\pi hc^2\lambda^{-5}}{1-[1-\varepsilon_s(\lambda)]R_c(\lambda)}\left[\frac{\varepsilon_s(\lambda)[1-R_c(\lambda)]}{\exp(hc/\lambda kT_s)-1}\right]d\lambda, \tag{6}$$

which can be further reduced to

$$q(\lambda)d\lambda = \frac{2\pi hc^2\lambda^{-5}[\exp(hc/\lambda kT_s)-1]^{-1}}{[\varepsilon_s(\lambda)]^{-1}+\{[R_c(\lambda)]^{-1}-1\}^{-1}}d\lambda. \tag{7}$$

Note that the converter reflectivity $R_C(\lambda)$ includes the effect of the spectrally selective filter, which plays a major role in determining the system efficiency of the generator.

The energy flux absorbed by the converter is in the form of photons. Since each photon has an energy $h\nu = hc/\lambda$, the absorbed photon flux $\phi_p(\lambda)d\lambda$ in the wavelength interval λ to $\lambda + d\lambda$ is given by

$$\phi_p(\lambda)d\lambda = \frac{2\pi\alpha c\lambda^{-4}[\exp(hc/\lambda kT_s)-1]^{-1}}{[\varepsilon_s(\lambda)]^{-1}+\{[R_c(\lambda)]^{-1}-1\}^{-1}}d\lambda \tag{8}$$

where α is the fraction of the converter area covered by active photovoltaic cells. These convert the absorbed photons into an electron flux $\phi_e(\lambda)d\lambda$ with a wavelength-dependent quantum efficiency $Q(\lambda)$.

$$\phi_e(\lambda)d\lambda = \phi_p(\lambda)Q(\lambda)d\lambda \tag{9}$$

Thus, the converter's short-circuit current density J_{sc} is given by

$$J_{sc} = e\int_0^\infty \phi_p(\lambda)Q(\lambda)d\lambda, \tag{10}$$

where e is the electronic charge.

Inserting Eqs. (8) and (9) into (10), the short-circuit current density J_{sc} is given by

$$J_{sc} = 2\pi\alpha ce\int_0^\infty \frac{\lambda^{-4}Q(\lambda)[\exp(hc/\lambda kT_s)-1]^{-1}}{[\varepsilon_s(\lambda)]^{-1}+\{[R_c(\lambda)]^{-1}-1\}^{-1}}d\lambda. \tag{11}$$

The open-circuit voltage V_{oc} of each photovoltaic cell is given by

$$V_{oc} = (kT_c/e)\ln[(J_{sc}/J_o)-1], \tag{12}$$

where J_o is the saturation current density of the photovoltaic material. According to Boeing investigators, the value of J_o is given by

$$J_o = [2.555x10^{-4}T_c^3\exp(-E_g/kT_c)] \text{ amps/cm}^2, \tag{13}$$

where the energy gap E_g for gallium antimonide is given by

$$E_g = [0.7-3.7x10^{-4}(T_c-300^o K)] \text{ electron volts.} \tag{14}$$

The short-circuit current density J_{sc} and the open-circuit cell voltage V_{oc} can be used to compute the converter's maximum power output density

$$P_{\max} = J_{sc}V_{oc}F, \tag{15}$$

where **F** is the fill factor, given by

$$F = \{1-[\ln(J_{sc}/J_o)]^{-1}\}\{1-\ln[\ln(J_{sc}/J_o)][\ln(J_{sc}/J_o)]^{-1}\}. \tag{16}$$

In designing the generator, we have assumed that at the maximum power point

$$J/J_{sc} = F^{1/3}, \tag{17}$$

$$V/V_{oc} = F^{2/3}, \tag{18}$$

which seems to be in good agreement with experimental data.

In applying the above series of equations, we require three sets of experimentally determined data: the heat source emissivity $\varepsilon_s(\lambda)$, the converter/filter reflectivity $R_C(\lambda)$, and the converter's quantum efficiency $Q(\lambda)$. The first set was obtained from a handbook [13], and the latter two sets were supplied to us by Boeing investigators (E. Horne, M. Morgan). As shown in Table 1, their data is given in terms of the wave number ω, the reciprocal of the wavelength λ. Therefore, it is convenient to recast Eq. (11) in terms of wave number:

$$J_{sc} = 2\pi\alpha c e \int_0^\infty \frac{\omega^2 Q(\omega)[\exp(hc\omega/kT_s)-1]^{-1}}{[\varepsilon_s(\omega)]^{-1}+\{[R_c(\omega)]^{-1}-1\}^{-1}}\, d\omega. \tag{19}$$

Two sets of data are listed in Table 1 for the filter's spectral reflectivity **$R_c(\omega)$** and the cell's quantum efficiency ***$Q(\omega)$***. For each property, the more conservative measured data set (M) is based on measurements of already fabricated non-optimized samples made by Boeing investigators for other applications, and the "improved" or "projected" data set (P) is based on their estimates of what improvements could be achieved by known stratagems for optimizing the filter and the photovoltaic cells for the present RTPV application. The illustrative example described in this section is based on the improved properties set, but later sections that summarize the results of our integrated RTPV system studies present results for both the more conservative measured performance parameters and the predicted improved properties. Our studies showed that the projected improvements in quantum efficiency had only a minor effect on system performance, but that the improved filter characteristics had a pronounced effect.

Table 1 Spectral Transmittance of Filter (AuC-2) and Quantum Efficiency of PV Cell (GaSb)

$\omega = 1/\lambda$

M = Measured
P = Projected

ω cm^{-1}	$1-R_c(\omega)$		$Q(\omega)$	
	M	**P**	**M**	**P**
100	0.03	0.02	0.00	0.00
200	0.03	0.02	0.00	0.00
300	0.03	0.02	0.00	0.00
400	0.03	0.02	0.00	0.00
500	0.03	0.02	0.00	0.00
600	0.03	0.02	0.00	0.00
700	0.03	0.02	0.00	0.00
800	0.03	0.02	0.00	0.00
900	0.03	0.02	0.00	0.00
1000	0.03	0.02	0.00	0.00
1100	0.03	0.02	0.00	0.00
1200	0.03	0.02	0.00	0.00
1300	0.03	0.02	0.00	0.00
1400	0.03	0.02	0.00	0.00
1500	0.03	0.02	0.00	0.00
1600	0.03	0.02	0.00	0.00
1700	0.03	0.02	0.00	0.00
1800	0.03	0.02	0.00	0.00
1900	0.03	0.02	0.00	0.00
2000	0.03	0.02	0.00	0.00
2100	0.035	0.02	0.00	0.00
2200	0.035	0.02	0.00	0.00
2300	0.035	0.02	0.00	0.00
2400	0.035	0.02	0.00	0.00
2500	0.035	0.02	0.00	0.00
2600	0.035	0.02	0.00	0.00
2700	0.035	0.02	0.00	0.00
2800	0.035	0.02	0.00	0.00
2900	0.04	0.02	0.00	0.00
3000	0.04	0.02	0.00	0.00
3100	0.04	0.02	0.00	0.00
3200	0.04	0.02	0.00	0.00
3300	0.04	0.02	0.00	0.00
3400	0.05	0.02	0.00	0.00
3500	0.05	0.02	0.00	0.00
3600	0.05	0.02	0.00	0.00
3700	0.055	0.02	0.00	0.00
3800	0.055	0.02	0.00	0.00
3900	0.055	0.02	0.00	0.00
4000	0.06	0.02	0.00	0.00
4100	0.06	0.02	0.00	0.00
4200	0.065	0.02	0.00	0.00
4300	0.077	0.02	0.00	0.00
4400	0.08	0.02	0.00	0.00
4500	0.086	0.02	0.00	0.00
4600	0.097	0.02	0.00	0.00
4700	0.1	0.02	0.00	0.00
4800	0.112	0.02	0.00	0.00
4900	0.13	0.02	0.00	0.00
5000	0.14	0.02	0.00	0.00
5100	0.15	0.02	0.00	0.00
5200	0.17	0.03	0.00	0.00
5300	0.183	0.04	0.00	0.00
5400	0.205	0.055	0.00	0.00

ω cm^{-1}	$1-R_c(\omega)$		$Q(\omega)$	
	M	**P**	**M**	**P**
5500	0.23	0.08	0.10	0.11
5600	0.255	0.11	0.24	0.26
5700	0.3	0.14	0.45	0.49
5800	0.325	0.16	0.55	0.60
5900	0.368	0.21	0.65	0.71
6000	0.377	0.25	0.67	0.73
6100	0.411	0.3	0.71	0.78
6200	0.45	0.34	0.73	0.79
6300	0.47	0.4	0.74	0.81
6400	0.49	0.47	0.75	0.82
6500	0.51	0.53	0.76	0.83
6600	0.523	0.6	0.77	0.84
6700	0.532	0.665	0.78	0.85
6800	0.54	0.725	0.78	0.85
6900	0.543	0.81	0.79	0.86
7000	0.54	0.83	0.79	0.85
7100	0.534	0.85	0.80	0.86
7200	0.528	0.84	0.80	0.86
7300	0.51	0.835	0.81	0.87
7400	0.49	0.795	0.81	0.87
7500	0.47	0.745	0.81	0.87
7600	0.443	0.695	0.81	0.87
7700	0.42	0.64	0.82	0.86
7800	0.39	0.56	0.82	0.86
7900	0.365	0.48	0.82	0.85
8000	0.34	0.41	0.82	0.85
8100	0.308	0.375	0.82	0.85
8200	0.28	0.35	0.82	0.85
8300	0.25	0.32	0.83	0.85
8400	0.23	0.29	0.83	0.84
8500	0.208	0.275	0.83	0.84
8600	0.19	0.26	0.83	0.83
8700	0.176	0.25	0.83	0.83
8800	0.158	0.24	0.82	0.83
8900	0.14	0.235	0.82	0.82
9000	0.13	0.23	0.82	0.81
9100	0.118	0.225	0.82	0.81
9200	0.1	0.225	0.82	0.80
9300	0.092	0.22	0.82	0.80
9400	0.08	0.22	0.82	0.78
9500	0.07	0.215	0.82	0.77
9600	0.06	0.21	0.81	0.76
9700	0.055	0.205	0.80	0.75
9800	0.05	0.2	0.80	0.74
9900	0.04	0.2	0.79	0.73
10000	0.035	0.195	0.78	0.71
10100	0.03	0.1875	0.77	0.70
10200	0.025	0.18	0.76	0.69
10300	0.023	0.1766	0.75	0.69
10400	0.021	0.1733	0.75	0.69
10500	0.02	0.17	0.74	0.68
10600	0.02	0.1666	0.73	0.67
10700	0.017	0.1633	0.72	0.66
10800	0.016	0.16	0.71	0.65

ω cm^{-1}	$1-R_c(\omega)$		$Q(\omega)$	
	M	**P**	**M**	**P**
10900	0.02	0.157	0.70	0.64
11000	0.02	0.156	0.70	0.64
11100	0.025	0.155	0.69	0.63
11200	0.03	0.15	0.68	0.62
11300	0.035	0.15	0.67	0.61
11400	0.04	0.1	0.66	0.60
11500	0.05	0.1	0.65	0.59
11600	0.052	0.1	0.64	0.58
11700	0.053	0.1	0.63	0.58
11800	0.055	0.1	0.62	0.57
11900	0.056	0.1	0.61	0.56
12000	0.057	0.1	0.60	0.55
12300	0.055	0.1	0.60	0.55
12600	0.05	0.1	0.58	0.53
12900	0.045	0.1	0.56	0.51
13200	0.04	0.1	0.54	0.49
13500	0.04	0.1	0.52	0.49
13800	0.035	0.1	0.50	0.48
14100	0.03	0.1	0.48	0.47
14400	0.05	0.1	0.46	0.46
14700	0.05	0.1	0.45	0.46
15000	0.05	0.1	0.44	0.46
15300	0.05	0.1	0.43	0.46
15600	0.05	0.1	0.42	0.46
15900	0.05	0.1	0.40	0.45
16200	0.05	0.1	0.38	0.45
16500	0.05	0.1	0.36	0.44
16800	0.05	0.1	0.34	0.42
17100	0.05	0.1	0.32	0.40
17400	0.05	0.1	0.31	0.38
17700	0.05	0.1	0.30	0.37
18000	0.05	0.1	0.30	0.37
18300	0.05	0.1	0.30	0.37
18600	0.05	0.1	0.30	0.37
18900	0.05	0.1	0.32	0.40
19200	0.05	0.1	0.35	0.43
19500	0.05	0.1	0.38	0.47
19800	0.05	0.1	0.40	0.50
20100	0.05	0.1	0.41	0.43
20400	0.05	0.1	0.42	0.44
20700	0.05	0.1	0.43	0.45
21000	0.05	0.1	0.44	0.46
21300	0.05	0.1	0.45	0.47
21600	0.05	0.1	0.46	0.48
21900	0.05	0.1	0.47	0.49
22200	0.05	0.1	0.48	0.50
22500	0.05	0.1	0.50	0.53
22800	0.05	0.1	0.50	0.53
23100	0.05	0.1	0.50	0.53
23400	0.05	0.1	0.48	0.50
23700	0.05	0.1	0.46	0.48
24000	0.05	0.1	0.43	0.45
24300	0.05	0.1	0.40	0.42
24600	0.05	0.1	0.36	0.38
24900	0.05	0.1	0.36	0.38

Illustrative Example

To illustrate the application of the above-derived equations, consider a heat source enclosed in a smooth tungsten-coated canister with the handbook-given [13] values of spectral emissivity $\varepsilon(\lambda)$ depicted by the solid curve of Figure 11. The canister operates at an illustrative temperature T_S = 1150°C = 1423°K, and radiates to a spectral filter and gallium antimonide photovoltaic cells at a converter temperature of T_C=0°C=273°K with an active area fraction $\alpha = 0.90$.

Fig. 11 Spectral Emissivity of Tungsten Canister

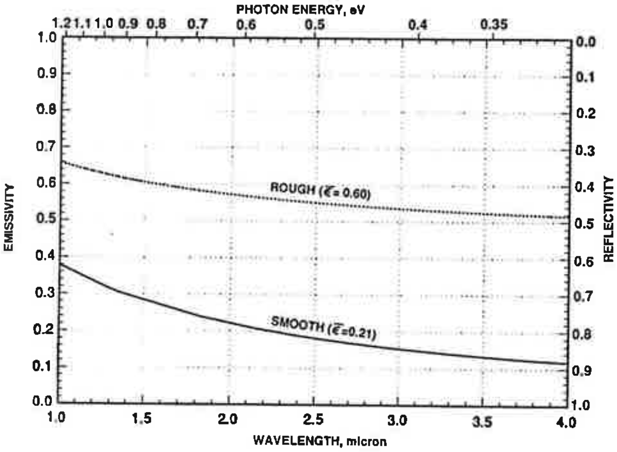

Fig. 12 Emission of Black Body and of Tungsten Canister (1150°C) and Absorption of Filtered Converter (0°C)

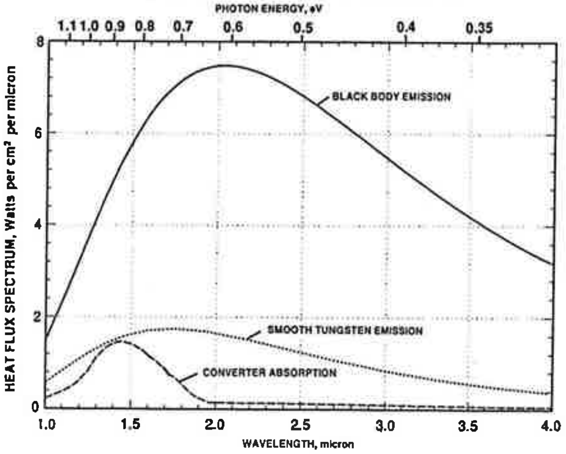

For the above temperatures, Figure 12 shows the spectral variation of the black-body radiation rate (Eq. 1), the radiative heat flux emitted by the smooth tungsten heat source canister (Eq. 2), and the net heat flux radiated from the canister to the filtered converter (Eq. 7). The difference between the tungsten emission curve and the converter absorption curve represents the effect of the spectral filter. As can be seen, at higher wavelengths most of the emitted radiation is reflected back to the heat source by the filter.

Figure 13 shows the photon flux absorbed by the filtered converter (Eq. 8), and the corresponding electron flux generated in the photovoltaic cells (Eq. 9). At each wavelength, the ratio of electron flux to photon flux represents the quantum efficiency of the gallium antimonide cells. As can be seen, at the shorter wavelengths or higher photon energies, the two curves are close together, indicating high quantum efficiencies. But at the higher wavelengths the two curves diverge, indicating poor quantum efficiencies of the GaSb cell, i.e., poor ability to convert absorbed protons into electrons. That is why the filter which reflects those wavelengths back to the heat source before they reach the PV cells is so beneficial to the converter's efficiency.

Fig. 13 Illustrative Example: Absorbed Photon Flux and Generated Electron Flux Spectra

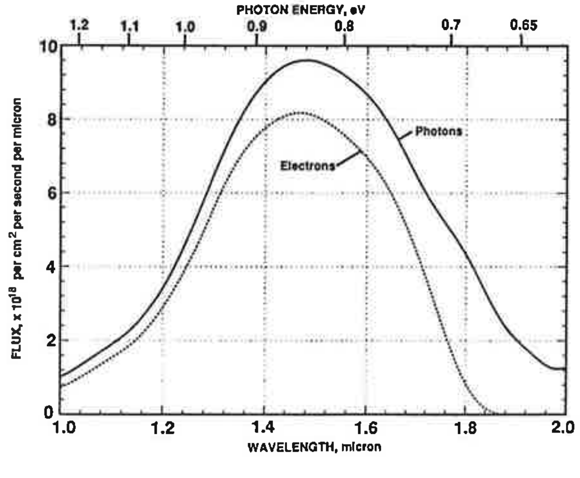

Applying numerical integration over the range of wavelengths to the illustrative example:

Eq. (9) gives the net heat flux absorbed by the converter $q_{net} = 0.99$ watt/cm^2,

Eq. (11) gives the short-circuit current density $J_{sc} = 0.62$ amp/cm^2,

Eqs. (12, 13, 14) give the open-circuit voltage $V_{oc} = 0.50$ volt,

Eq. (16) gives the fill factor $F = 0.82$,

Eq. (15) gives the maximum power density of the converter $P_{max} = 0.25$ watt/cm^2,

Eqs. (17) and (18) give the current density $J = 0.58$ amp/cm^2 and cell voltage $V = 0.44$ volt,

and the corresponding converter efficiency is $\eta = P_{max}/q_{net} = 25.2\%$.

Similar numerical integrations were carried out for a range of heat source temperatures T_s and converter temperatures T_c, with the parametric results displayed in Figures 14 through 17. Figure 14 shows that the net heat flux is only a function of the source temperature, and is essentially independent of the cell temperature in the range of interest.

Figures 15 and 16 show that the output power density and the converter efficiency are sensitive functions of the cell temperature. Lowering that temperature leads to significant performance improvements, albeit at the cost of increased radiator mass. Trade-offs between those parameters to maximize the system's specific power are described in a later section.

Fig. 14 Effect of Source Temperature on Net Heat Flux Absorbed by Converter

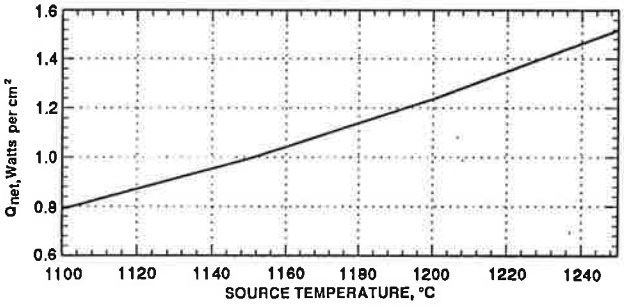

Fig. 15 Effect of Source and Cell Temperatures on Maximum Output Power Density of Converter

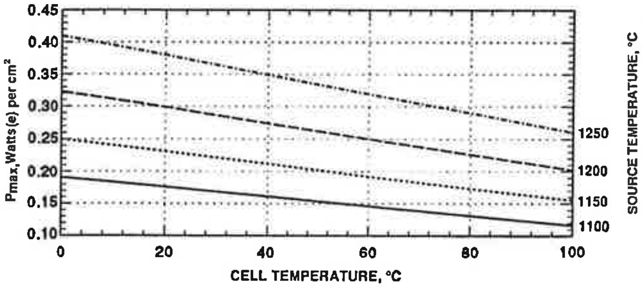

Fig. 16 Effect of Source and Cell Temperatures on Efficiency of Converter

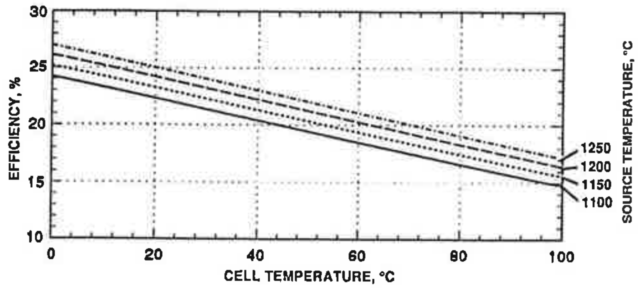

The results of Figures 14, 15, and 16 are combined in Figure 17, which presents cross-plots showing the effect of q_{net} on T_s, P_{max}, and η, for a range of cell temperatures T_c. It again shows the performance improvement obtainable by lowering the cell temperature.

Fig. 17 Effect of Net Heat Flux and Cell Temperature on Source Temperature, Power Density, and Efficiency

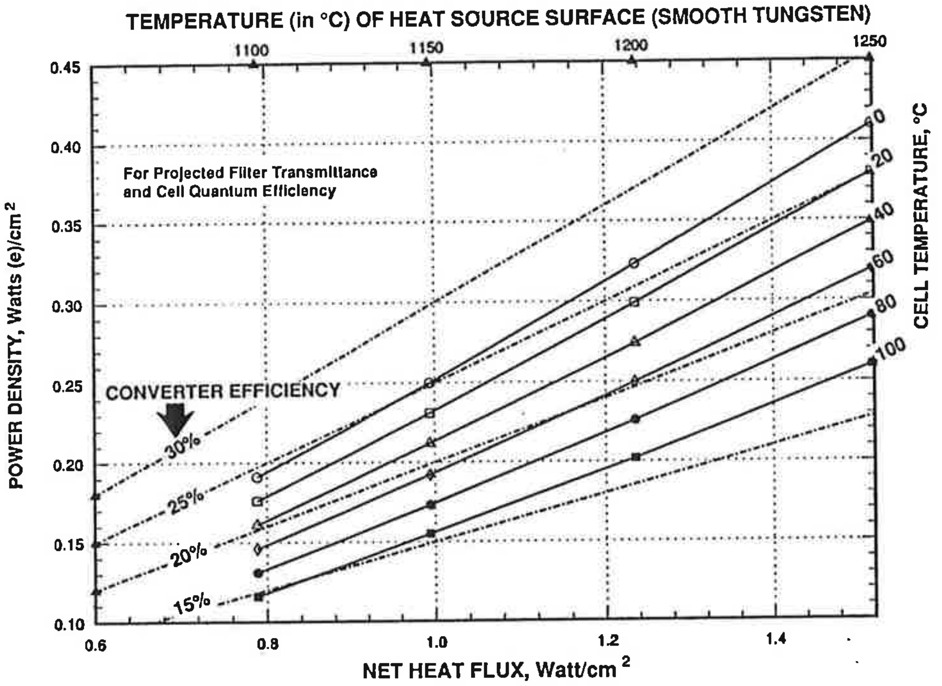

Figure 17 also shows that, for a given heat flux, higher source temperatures lead to higher power densities and efficiencies. From that, one might infer that these parameters can be significantly increased by lowering the heat source emissivity, which raises the source temperature for a given heat flux. But quite the opposite was found to be the case. This was discovered in the Fairchild study when the effect of roughening the tungsten surface on the converter's performance was analyzed.

The effective total emissivity, $\overline{\varepsilon_s}$ of the heat source canister is obtained by a weighted average of its spectral emissivity $\varepsilon_s(\lambda)$:

$$\overline{\varepsilon_s} = \frac{\int_o^\infty \lambda^{-5}[\exp(hc/\lambda kT_s)-1]^{-1}\varepsilon_s(\lambda)d\lambda}{\int_o^\infty \lambda^{-5}[\exp(hc/\lambda kT_s)-1]^{-1}d\lambda} \qquad (20)$$

Applying the spectral emissivities for smooth tungsten shown by the solid curve in Figure 11 gives a value of 0.21 for $\overline{\varepsilon_s}$. It was assumed that roughening the tungsten (e.g., by grit blasting) would raise its effective total emissivity to 0.60. This corresponds to a 45% reduction of the smooth-tungsten spectral reflectivity $[1-\varepsilon_s(\lambda)]$, resulting in the spectral emissivity for roughened tungsten shown by the dashed curve of Figure 11.

The effect of that emissivity increase is shown in Figure 18, which compares the converter's computed performance for smooth and roughened canisters at a 0°C cell temperature. As can be seen, for the same heat flux the roughened canister actually yields a somewhat higher power density and converter efficiency, contrary to expectations. Most important, it does so at an appreciably lower heat source temperature (by almost 100°C). Since lowering the heat source temperature without loss of performance is a desirable goal, the balance of our RTPV design study assumed the use of a roughened tungsten canister.

Fig. 18 Effect of Canister Roughness on its Temperature, Converter Efficiency, and Output Power

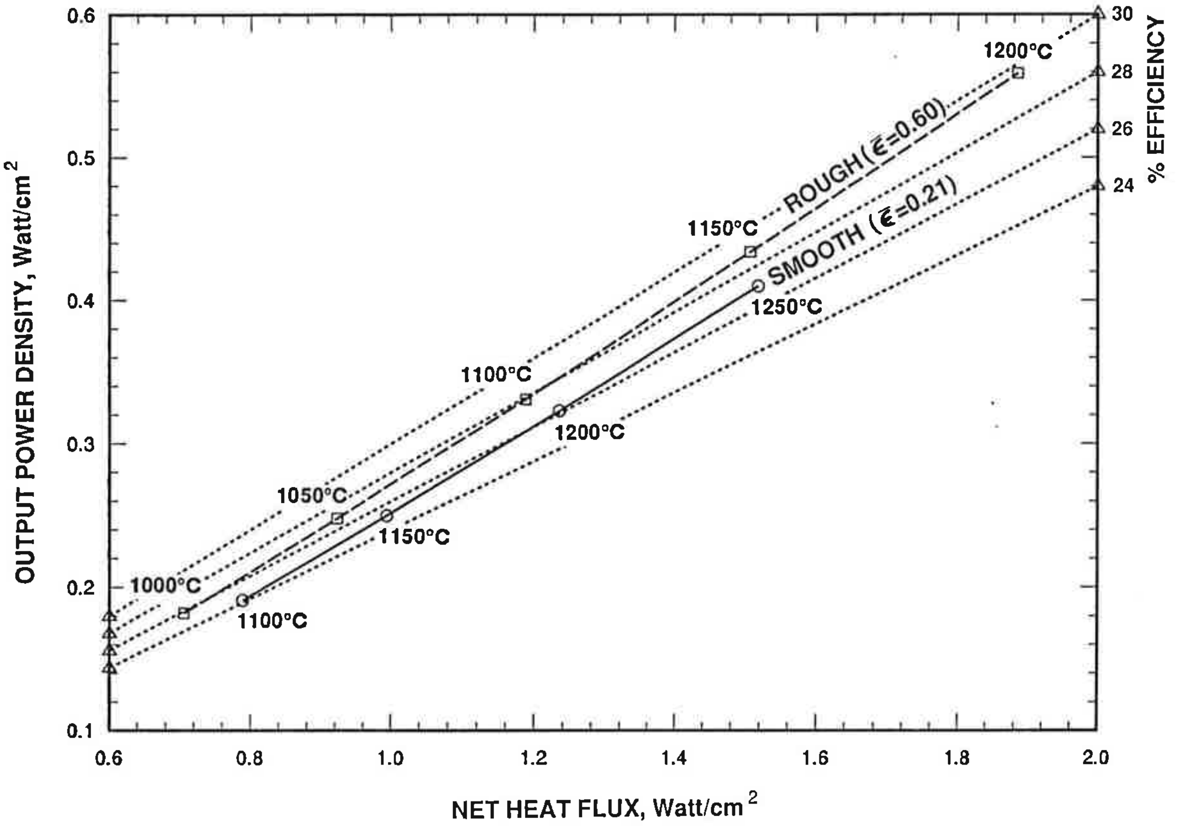

System Analysis

Determining the optimum system design, particularly the fin design that maximizes the system's specific power, requires a coupled thermal and electrical analysis. In that analysis, the heat generation rate is known, but the heat source surface temperature T_s and cell temperature T_c are not. Therefore, the analysis must be carried out iteratively. The coupled analysis was carried out by means of a thermal analysis code, (SINDA [18]), that had been modified by Fairchild, and by a standard thermal radiation code, (SSPTA [19]). For the former we constructed a 197-node model, and for the latter a model consisting of 496 surfaces.

Fairchild made two major modifications in the thermal analysis code. The net heat flux q_{net} from the sides of the heat source to the converter cells at each iteration was computed by integration of Eq. (7),

$$q_{net} = 2\pi hc^2 \int_0^\infty \frac{\lambda^{-5}[\exp(hc/\lambda kT_s)-1]^{-1}}{[\varepsilon_s(\lambda)]^{-1}+\{[R_c(\lambda)]^{-1}-1\}^{-1}} d\lambda, \tag{21}$$

with appropriate corrections for gaps between cells and obstruction by the electrical grid; and the waste heat flowing to the radiator fins was computed by subtracting the converter's electrical power generation rate from the heat generation rate of the heat source. The power generation rate was computed by multiplying the total cell area of the generator by the power density P_{max} obtained from Eqs. (11) through (16). The two thermal codes computed a new set of canister and cell temperatures, which were used as inputs in the next iteration. This iterative procedure was repeated until the modified code converged on a consistent solution.

Structural Analysis

Before applying the above procedure to optimize the system design, we must first perform a static and dynamic structural analysis of the radiator to ensure that the long fins required for the desired low cell temperatures can survive the predicted launch loads without excessive stresses in their aluminum skins. In our structural analysis we assumed that the graphite skin contributes zero strength in the direction normal to the fibers.

Consider a fin of root-to-tip length x_1, honeycomb thickness z_o, and height y varying from y_o at the fin tip to y_1 at the fin root. Let x denote the horizontal distance from the fin tip. Then the fin height y at position x is given by

$$y = y_o - x(y_o - y_1)/x_1 = y_o - y'x, \tag{22}$$

where y' is defined as $(y_o - y_1)/x_1$.

The total mass dm of the fin segment between x and $x + dx$ is given by

$$dm = [2m_1 + m_2 y + 2m_3 y t_o]dx, \tag{23}$$

where m_1 is the mass per unit length of each heat pipe, m_2 is the mass per unit area of the honeycomb plus that of the two graphite skins and of the bond between them, m_3 is the volumetric density of the aluminum skins, and t_o is the thickness of each aluminum skin. Combining Eqs. (22) and (23), we obtain

$$dm = [2m_1 + (m_2 + 2m_3 t_o)(y_o - y'x)]dx. \tag{24}$$

When the fin is subjected to an acceleration load of magnitude **g** normal to its surface, the resultant bending moment **M** at position **x** is given by

$$M = g\int_{o}^{x}(x-x')[2m_1+(m_2+2m_3t_o)(y_o-y'x')]dx', \tag{25}$$

where **x'** is the variable of integration. Integrating Eq. (24) from $x'=0$ to $x'=x$, we obtain

$$M = g[m_1x^2+(m_2+2m_3t_o)(\tfrac{1}{2}y_ox^2-\tfrac{1}{6}y'x^3)]. \tag{26}$$

The maximum tensile stress **σ** in the aluminum fin at position **x** is given by

$$\sigma = (\tfrac{1}{2}z)M/I, \tag{27}$$

where **I**, the combined moment of inertia of the aluminum skins and the heat pipes at position **x**, is given by

$$I = \tfrac{1}{12}y[(z+2t_o)^3-z^3]+2I_o, \tag{28}$$

and where **I_o** is the moment of inertia of each heat pipe. Assuming that each heat pipe has a rectangular cross-section of base width **b**, depth z, and wall thickness **w**, its moment of inertia is given by

$$I_o = \tfrac{1}{12}[bz^3-(b-2w)(z-2w)^3]. \tag{29}$$

Since the aluminum skin thickness **t_o** is much smaller than the honeycomb thickness z, Eq. (28) reduces to

$$I = \tfrac{1}{2}yz^2t_o+2I_o. \tag{30}$$

Inserting Eqs. (26) and (30) into (27), the maximum tensile stress σ at position **x** is given by

$$\sigma = \frac{g[(m_1+\tfrac{1}{2}m_2y_o+m_3y_ot_o)x^2-\tfrac{1}{6}(m_2+2m_3t_o)y'x^3]}{(y_o-y'x)zt_o+4I_o/z}. \tag{31}$$

As an illustrative example, consider a fin of length **x_1**=30", thickness **z**=0.5", fin tip height **y_o**=20", fin root height **y_1**=5.0", and graphite thickness of 0.005". (As will later be shown, the generator's specific power is maximized with very thin graphite skins.) Assume that the heat pipe mass **m_1** per unit length is 1.61 g/cm; that the mass per unit area of the honeycomb is 0.063 g/cm^2, that of each 0.005" graphite skin is 0.025 g/cm^2; that of each bond layer is 0.022 g/cm^2, so that the areal density **m_2** is 0.157 g/cm^2; that the volumetric density **m_3** of the aluminum skins is 2.77 g/cm^3; and that the fin is subjected to quasi-static acceleration of 40 g or 392 m/s^2 normal to its surface. This last assumption was made because previous RTGs [14] were designed and qualification-tested to 40 g, but it is quite conservative for the present application, because the RTPV under study is much shorter than the RTGs, and because a quasi-static test may inherently be an overconservative representation of the dynamic launch loads.

For the above parameters, Figure 19 presents stress profiles computed from Eq. (30) for aluminum skin thicknesses t_o ranging from 0.003" to 0.010". As can be seen, decreasing the skin thickness increases the stress, but not very much because the effect of the smaller cross-sectional area is largely compensated by the reduced fin weight.

Fig. 19 Tensile Stress Profile Produced by 40-G Side Load on Fin with 20" Tip Height, 4.7" Base Height

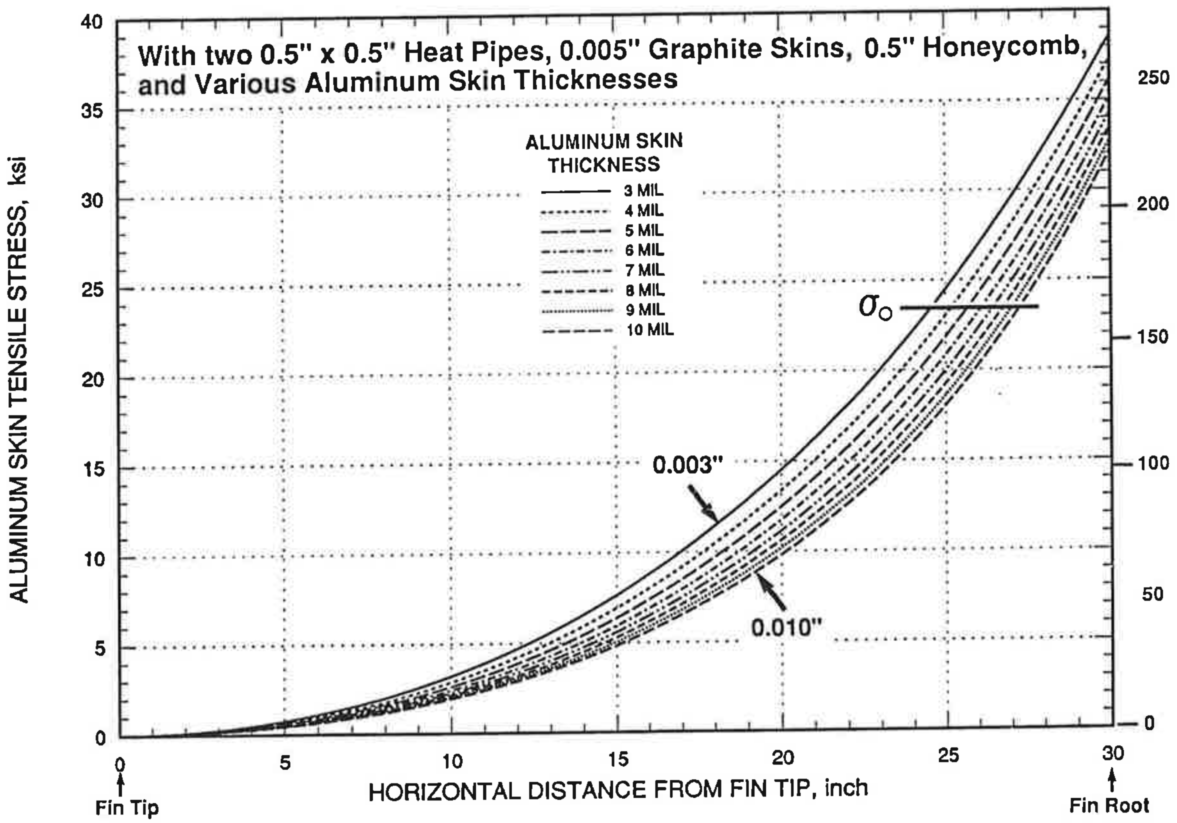

Let σ_o denote the maximum allowable tensile stress in the aluminum alloy. For a yield stress of 35 ksi, a safety factor of 1.5 gives an allowable stress of 23 ksi or 159 MPa. As can be seen, over most of the fin length the computed maximum stress displayed in Figure 19 is less than the allowable stress. Even for the thinnest aluminum skin (0.003") this is true for 24" of the 30" fin length. But near the fin root, the skin stress exceeds the allowable limit. To avoid this, the skin thickness must be gradually increased near the fin root.

In general, the maximum stress σ_1 at the fin root ($x=x_1$) for a uniform skin thickness t_o is

$$\sigma_1 = \frac{g[(m_1 + \tfrac{1}{2}m_2 y_o + m_3 y_o t_o)x_1^2 - \tfrac{1}{6}(m_2 + 2m_3 t_o)y' x_1^3]}{y_1 z t_o + 4I_o/z}. \qquad (32)$$

If $\sigma_1 < \sigma_0$, the fin can use a uniform skin thickness t_0 without exceeding the allowable stress limit σ_0. But if $\sigma_1 > \sigma_0$, the skin thickness near the fin root must be increased to avoid excessive stress. For that case, the cross-over point x_0 beyond which the assumed skin thickness t_0 is inadequate can be obtained by setting σ equal to σ_0 in Eq. (31) and solving the resultant cubic equation for x_0:

$$[\tfrac{1}{6}g(m_2+2m_3t_o)y']x_o^3-[g(m_1+\tfrac{1}{2}m_2y_o+m_3y_ot_o)]x_o^2-[\sigma_oy'zt_o]x_o+\sigma_o[y_ozt_o+4I_o/z]=0 \quad (33)$$

For $x_0 < x < x_1$, the skin thickness t must be increased above t_0 to avoid excessive stress. The required value of t at position x is obtained from Eq. (31), by setting $\sigma = \sigma_0$ and solving for t_0 in the denominator:

$$t=\frac{g[(m_1+\tfrac{1}{2}m_2y_o+m_3y_ot_o)x^2-(\tfrac{1}{6}m_2+\tfrac{1}{3}m_3t_o)y'x^3]}{z\sigma_o(y_o-y'x)}-\frac{4I_o/z^2}{y_o-y'x}. \quad (34)$$

Note that Eq. (34) is not quite accurate, because it omits the additional moment due to the thickened skin near the fin root. But the error introduced by that omission was shown to be quite small, because where the skin is thickened the moment arm is short and the fin height is relatively small.

Since the stress profiles displayed in Figure 19 for the illustrative example exceed the allowable stress limit of 23 ksi at $x=x_1$, the aluminum skins near the fin root must be increased in accord with Eq. (33). This is illustrated in Figure 20 for a range of initial skin thicknesses ranging from 0.003" to 0.010".

Fig. 20 Required Aluminum Skin Thickness Profiles to Keep Tensile Stress Below 23 ksi

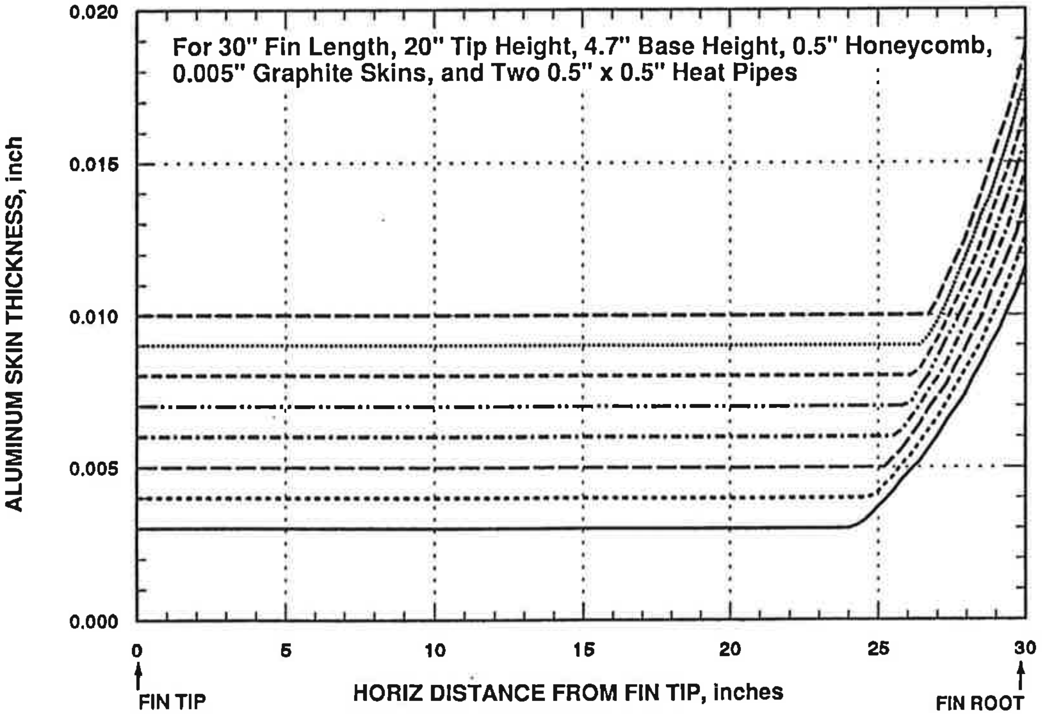

Figure 20 shows that, reducing the initial skin thickness will lighten the radiator even when the required skin thickening near the fin root is taken into account. Therefore, in our design study the aluminum skin thickness, except near the fin root, was fixed at 0.003", which was deemed the minimum practical thickness.

Figure 21 shows the required aluminum skin thickness at the fin root, for fin lengths ranging from 20" to 40", honeycomb thicknesses of 0.38" and 0.50", and skin thicknesses of 3 to 6 mils at the fin tips.

Fig. 21 Effect of Fin Length and Honeycomb Thickness on Required Aluminum Skin Thickness at Fin Root

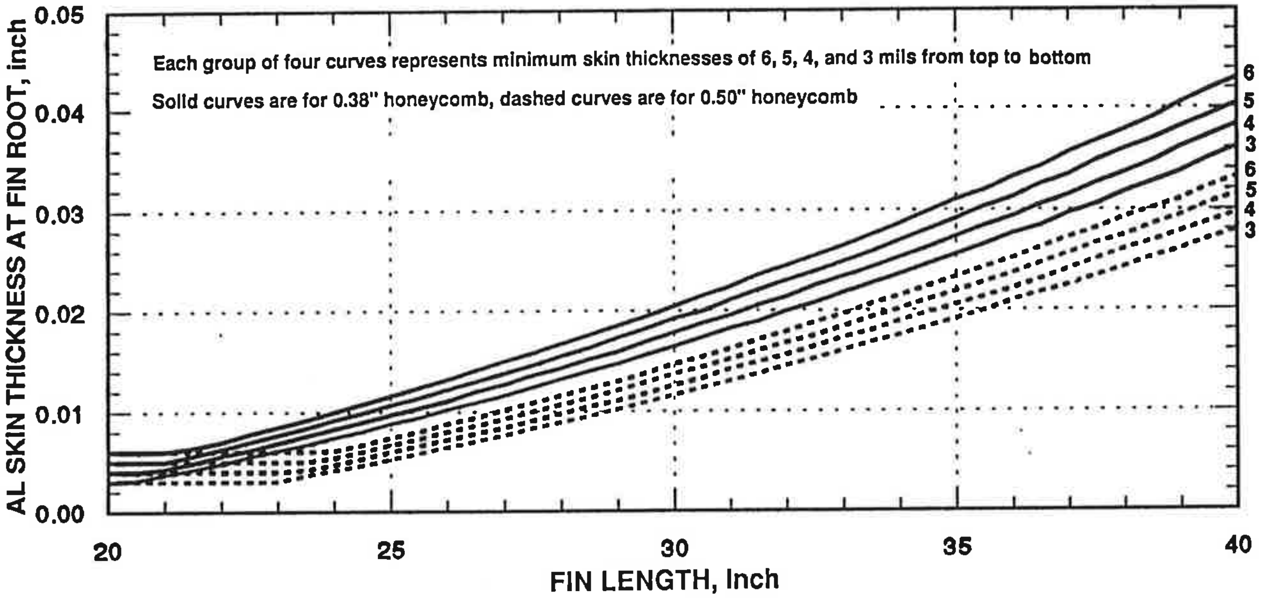

The figure shows that increasing the honeycomb thickness reduces the required skin thickness, as would be expected. However, the skin mass reduction must be traded off against the honeycomb mass increase. The mass ***m*** of the two aluminum skins on the fin segment projecting beyond the housing is given by

$$m = 2m_3 \int_o^{x_1} (y_o - y'x) t dx. \tag{35}$$

If $x_o > x_1$, the skin has a uniform thickness t_o, and its mass is given by

$$m = 2m_3 t_o [y_o x_1 - \tfrac{1}{2} y' x_1^2]. \tag{36}$$

If $x_o < x_1$, the skin thickness t between x_o and x_1 is increased, and the total skin mass m is given by

$$m = 2m_3 [t_o \int_o^{x_o} (y_o - y'x) dx + \int_{x_o}^{x_1} (y_o - y'x) t dx] \tag{37}$$

Combining Eqs (34) and (37), we obtain

$$m = 2m_3 t_o \int_{o}^{x_1} (y_o - y' x) dx$$
$$+ 2m_3 \int_{x_o}^{x_1} \{(g / z\sigma_o)[(m_1 + \tfrac{1}{2} m_2 y_o + m_3 y_o t_o) x^2 - (\tfrac{1}{6} m_2 + \tfrac{1}{3} m_3 t_o) y' x^3] - (4I_o / z^2)\} dx. \tag{38}$$

Finally, integration of Eq. (38) gives the aluminum skin mass per projecting fin:

$$m = 2m_3 \{t_o y_o x_o - \tfrac{1}{2} t_o y' x_o^2 - (4I_o / z^2)(x_1 - x_o)$$
$$+ (g / z\sigma_o)[\tfrac{1}{3}(m_1 + \tfrac{1}{2} m_2 y_o + m_3 y_o t_o)(x_1^3 - x_o^3) - \tfrac{1}{24}(m_2 + 2m_3 t_o) y' (x_1^4 - x_o^4)]\}. \tag{39}$$

From this, the total radiator mass for a given set of input parameters can be computed. This was done for fin lengths ranging from 20" to 40", for aluminum skin thicknesses (except near the fin roots) of 3, 4, 5, and 6 mils. The results for honeycomb thicknesses of 0.38" (solid curves) and 0.50" (dashed curves) are displayed in Figure 22, which shows the effect of fin length on the total radiator mass, including the thickened aluminum skins near the fin roots that are needed to avoid excessive stress.

Fig. 22 Effect of Fin Length and Honeycomb Thickness on Total Radiator Mass

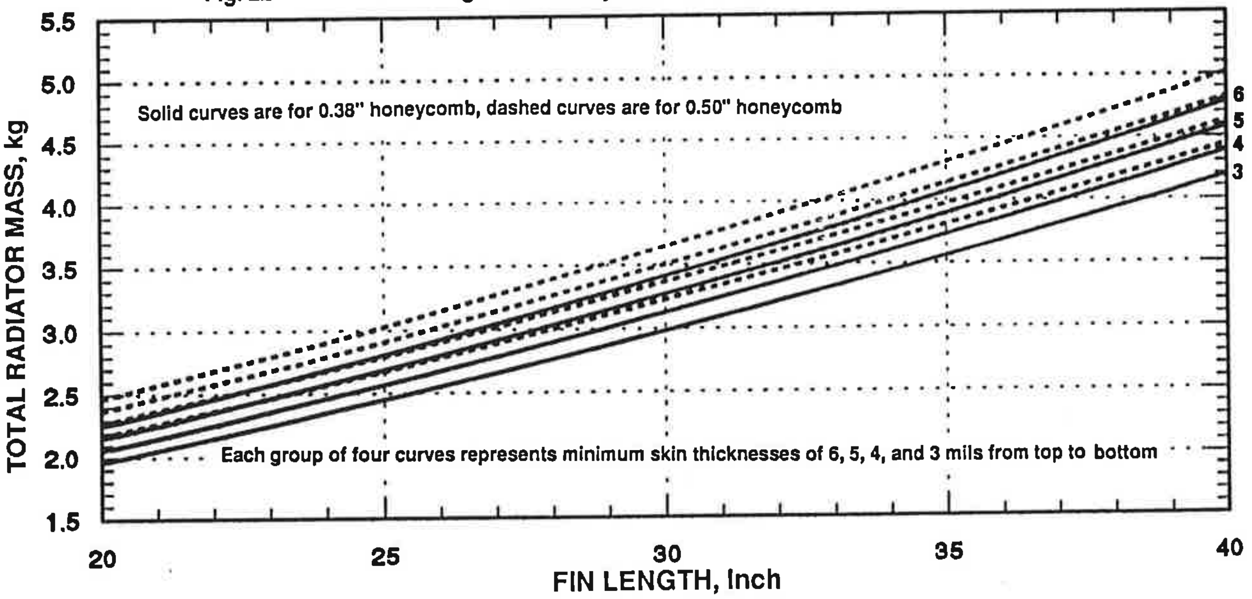

As was shown in Figure 21, increasing the honeycomb thickness reduces the required skin thickness. But Figure 22 shows that the resultant mass saving is less than the additional honeycomb mass. Consequently, the total radiator mass is somewhat lower for the 0.38" honeycomb than for the 0.50" thickness, and that thickness was adopted in our subsequent designs.

The preceding quasi-static analysis was supplemented by a dynamic analysis using a detailed NASTRAN [15] model of the radiator fin consisting of 966 nodes and 1717 elements. A plate element mesh was used for each of the two aluminum face sheets and for the two graphitized carbon-carbon sheets. The honeycomb core was modeled with four layers of solid elements, and the heat pipe walls were represented by a number of plate elements.

Since the graphitized carbon-carbon material is highly anisotropic, orthotropic material properties were used in the NASTRAN model. The modulus of elasticity in the vertical carbon fiber direction was assumed to be eight times larger than the modulus of elasticity in the fin length direction. The honeycomb core is also orthotropic and was assumed to have its higher shear strength L-direction (ribbon direction) oriented in the long fin direction, and its W-direction (transverse to the ribbon) parallel to the vertical axis.

Parametric studies were conducted on several fin configurations of interest. Each configuration was assessed by performing a modal analysis and using its results in a random analysis. The results were reassuring for the smaller fin sizes, but as the fin areas increased, so did concern about the possible acoustic response of the structure.

An acoustic analysis of one of the larger fin sizes (30" length by 20" tip height with a 0.5" honeycomb) was conducted using the VAPEPS (VibroAcoustic Payload Environment Prediction System) computer code [16]. VAPEPS is maintained and managed for NASA by JPL. In this analysis, four different qualification-level acoustic environments were used as input. They were the STS baseline 9' diameter payload, the STS maximum 15' diameter payload, the Titan III, and the Delta II vehicle with 10' fairing. The results of the four acoustic response analyses are plotted in Figure 23.

Fig. 23 Acoustic Response of 30" Radiator Fin for Various Launch Vehicles

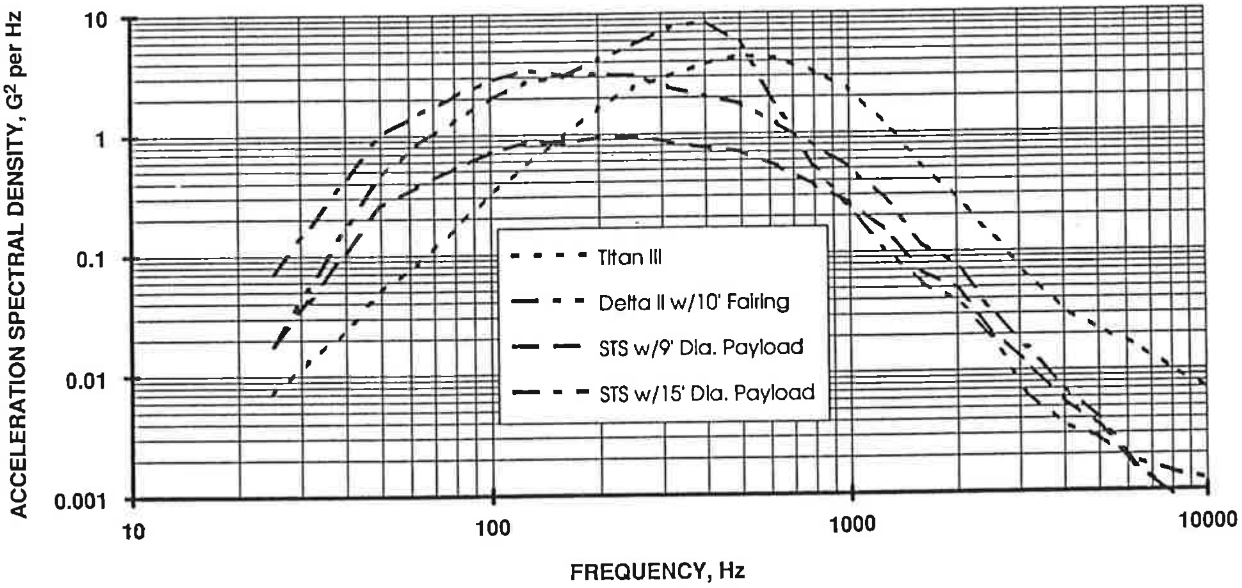

The above radiator configuration was analyzed for the acoustic response curve of the STS with a 9 ft diameter payload, since this is the most likely launch vehicle to be used for the Pluto Fast Flyby mission. (Another launch vehicle, the Russian Proton, is under active consideration, but an acoustic analysis of that option must await the availability of data similar to that used to generate Figure 23.) For the 11' STS option, an equivalent quasi-static pressure on the fin was calculated by summing the products of modal mass and dynamic force on a mode-by-mode basis. Stresses in the radiator fin due to the equivalent static pressure were then calculated. A 10-minute duration of the acoustic loading was assumed. An equivalent number of stress reversal cycles (184,378 cycles) for the radiator fin was derived from the modal participation data and the acoustic response curve. Finally, Miner's cumulative fatigue damage index [17] was calculated based on the S-N curves for 6061-T6 aluminum. The index sums the ratios of 1-, 2-, and 3-sigma stress reversal cycles to their corresponding allowable fatigue curve cycles. The results indicate that for the postulated launch vehicle, the 30"-long fin will satisfy Miner's fatigue requirement with ample margin (M.S. = +0.69).

Parametric System Analysis and Optimization

Let us first examine the effect of varying the graphite skin thickness on system characteristics for a set of illustrative parameters. For a 30" root-to-tip fin length, a 20" tip height, a 0.38" honeycomb thickness, a 0.003" aluminum skin thickness, and a converter with 90% active cell area, the effect of varying the graphite skin thickness from 0 to 0.030" is illustrated in Figure 24. The figure shows the effect of graphite skin thickness on system mass, cell temperature, output power, system efficiency, and specific power. In each of the three figures, the solid curve represents results based on measured values of filter transmittance and cell quantum efficiency, and the dashed curve is based on projected values as listed in Table I.

Fig. 24 Effect of Graphite Skin Thickness

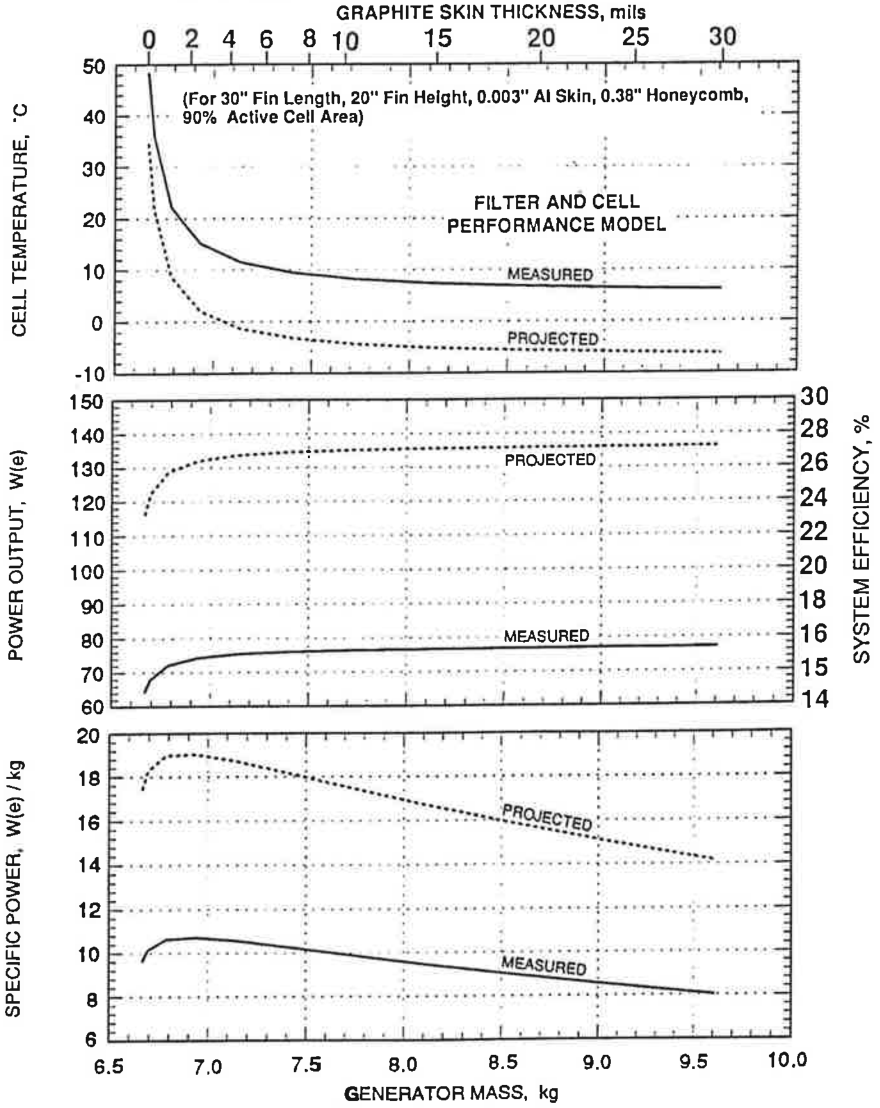

As shown in Figure 24, the projected properties (primarily the filter transmittance) have a pronounced effect on system performance. It is also noteworthy that initially the addition of the graphite skins benefits output power and efficiency significantly, but after adding a surprisingly small thickness (typically 0.005") further additions of graphite only increase the mass with little further increase of power or efficiency.

Similar analyses were carried out for fin lengths ranging from 20" to 40" and for fin tip heights of 12" and 20". The results for all cases showed similar trends, confirming the previous conclusion that the specific power of the design is maximized at a graphite skin thickness around 0.005". With thicker graphite skin, the increase in power output is quite small and is outweighed by the increased graphite mass.

The results of the parametric design studies are displayed in Figure 25 and 26. Both figures show curves representing the results of thermal, electrical, and mass analyses for fin lengths ranging 20" to 40" and fin tip heights ranging from 12" to 20", with the graphite skin thickness as the implicit variable within each curve. Each point on each curve is the result of an iterative solution of the coupled thermal and electrical analyses, using the modified thermal analysis code described earlier. All curves assume aluminum skins varying from 0.003" at the fin tip to whatever is needed near the fin root to survive a 40-g launch load without exceeding the 23 ksi allowable stress limit.

Figure 25 shows plots of cell temperature versus generator mass. For each fin size, the upper curve is based on the measured filter transmittance and PV quantum efficiency model, and the lower curve is for the projected improved filter and cell characteristics. As can be seen, the larger fins lead to very low cell temperatures, but at substantially higher masses.

Fig. 25 Effect of Fin Dimensions on Cell Temperature

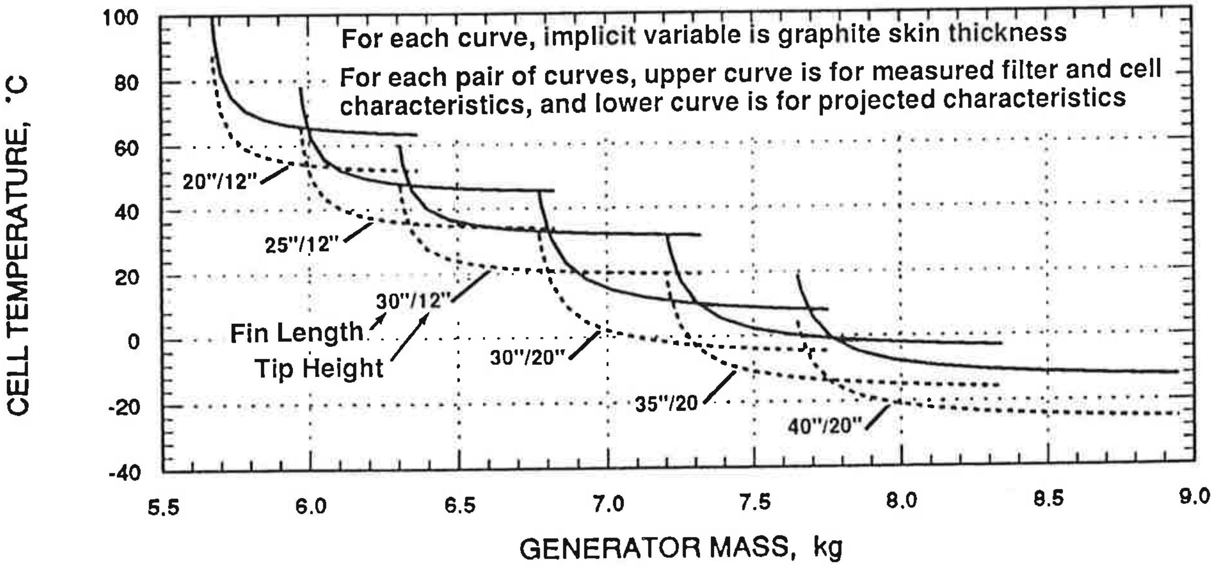

The trade-offs between mass and performance are summarized in Figure 26. For each fin size, it presents a curve of output power and system efficiency versus generator mass, with graphite skin thickness as the implicit variable. It also shows diagonal lines of constant specific power, which identify the fin dimensions that maximize the generator's specific power.

Fig. 26 BOM Power, System Efficiency, and Specific Power Versus Generator Mass (and Implicit Graphite Thickness)

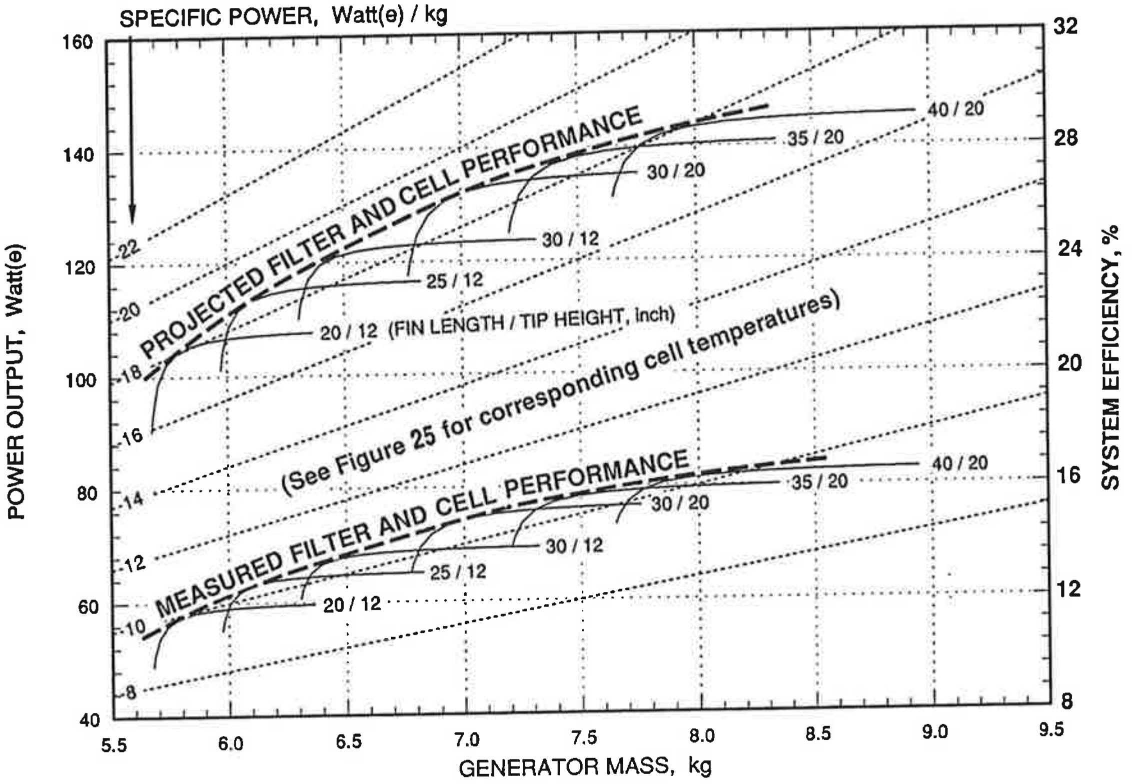

For the measured and projected filter and cell performance models, the figure shows a dashed envelope curve tangent to each family of performance curves for different fin dimensions. For each performance model, the corresponding envelope curve represents the highest specific power that can be achieved by optimizing the system's radiator geometry. For every point on the envelope, there is some combination of fin length, fin tip height, and graphite skin thickness that will achieve the indicated performance.

As can be seen, for both performance models the system's specific power is maximized with a 30" fin length and 20" fin height. But note that this optimum is quite broad. As illustrated in Table 2, major deviations from the optimum design result in only modest reductions in specific power. Thus, the designer has wide latitude in trading off power versus mass to meet specific mission goals. For example, for the projected filter and cell performance, the BOM power could be raised from 130 watts to 145 watts by lengthening the fins from 30" to 40". As shown, this would increase the generator's mass from 7.2 to 8.2 kg, but would only decrease its specific power from 18.6 to 17.6 w/kg. Conversely, if desired the generator mass could be reduced from 7.2 kg to 5.7 kg by reducing the fin size. As shown, this would reduce the BOM power from 130 watts to 103 watts, but would only lower the generator's specific power from 18.6 to 18.0 w/kg.

Table 2: Effect of Off-Optimum Design on RTPV Performance

Goal	Low Mass	Max Sp Power	High Power
Fin Length	20"	30"	40"
Fin Tip Height	12"	20"	20"
Cell Temperautre	68°C	0°C	-21°C
Power (BOM)	103 w	130 w	145 w
Efficiency (BOM)	20.6%	26.0%	29.0%
System Mass	5.7 kg	7.2 kg	8.2 kg
Specifc Power	18.0 w/kg	18.6 w/kg	17.6 w/kg

The optimum 30" fin length and 20" fin tip height were used in the RTPV design illustrations previously shown in Figures 8, 9, and 10. For those dimensions, Table 3 presents a detailed mass breakdown, and Table 4 lists key parameters of the RTPV system for both the measured and the projected models of filter transmittance and cell quantum efficiency. For comparative purposes, the tables also list the same parameters for a recently designed RTG [8] for the Pluto Fast Flyby mission:

Table 3: Comparative Mass Breakdown (kg)

Generator	RTG	RTPV
GPHS Modules		
Fuel (PuO_2)	2.98	1.19
Clads (Ir)	1.17	0.47
Graphitics	3.09	1.23
Canister (Mo)	0.00	0.63
Structural Supports	1.07	0.00
Multifoil Insulation (Mo)	1.44	0.09
Converter Elements, etc.	2.15	0.17
Housing, etc.	2.90	0.53
Radiator	1.56	2.85
TOTAL	15.36	7.16

As shown, the radiator mass is only 10% of the RTG mass but 40% of the RTPV mass. This confirms the importance of optimizing the RTPV's radiator design. The RTPV design - for both the measured and the projected performance models - offers very substantial mass improvements over the RTG. Its mass is less than half the RTG mass. It not only meets JPL's very ambitious mass reduction goal of 9.5 kg, but at 7.2 kg it greatly exceeds it. The requirements for the costly radioisotope fuel capsules is reduced by 60%, which can result in substantial cost reductions, since historically the fuel capsules and its graphitic enclosures are the dominant cost components of RTGs

For both the Measured and Projected filter and cell performance models, Table 4 compares the BOM operating temperatures and system characteristics of the RTPV with those of the RTG, and shows the effect of 9-year fuel decay on the RTPV's performance.

Table 4: RTG/RTPV BOM Performance Comparison and Effect of 9-year Fuel Decay

Generator	**RTG**	**RTPV**			
Mission Phase	**BOM**	**BOM**		**EOM***	
Performance Model	Unicouple	Measured	Projected	Measured	Projected
Generator Mass, kg	15.4	7.2	7.2	7.2	7.2
Number of Heat Source Modules	5	2	2	2	2
Thermal Power, watts	1250	500	500	465	465
Operating Temperatures, °C:					
Clad	1326	1153	1210	1132	1190
Aeroshell	1060	1062	1128	1045	1111
Canister	none	1034	1103	1018	1087
Converter	990/267	11	-2	-4	-8
Radiator Heatpipe	none	-9	-19	-14	-24
Output Voltage	19	26.5	28.6	26.7	28.6
Output Current, amps	4.6	2.9	4.7	2.6	4.4
Output Power, watts	87	76	134	71	126
System Efficiency, %	7.0	15.1	26.8	15.2	27.1
Specific Power, watts/kg	5.7	10.4	18.5	9.7	17.4

* Effect of fuel decay only, before correcting for radiation effects.

The computed 1128°C BOM aeroshell temperature for the projected filter and cell performance is somewhat above the corresponding 1100°C temperature in RTGs. But this does not matter, because the critical temperature is not the aeroshell's but the clad's. Excessive clad temperatures can lead to grain growth and embrittlement of the iridium alloy, which can lead to clad breach in case of inadvertent earth impact. The computed RTPV clad temperature of 1210°C is well below the 1300°C clad temperature in previous RTGs. This is because the presence of helium within the RTPV canister reduces the normal temperature drops between the clad and the aeroshell. In addition, a separate analysis showed that loss of helium from the canister would only result in a clad temperature rise to 1305°C, which is still within the prescribed clad temperature limit of 1330°C. This is important, because it means that the reliability and safety of the RTPV are not dependent on retaining the hermeticity of the canister.

The RTPV's converter temperature is much lower than that of the RTG. This should eliminate the temperature-induced degradation effects found in thermoelectric converters.

Comparison of the BOM and EOM columns shows that 9-year fuel decay drops the canister temperature by 16°C and the cell temperature by 6°C. This reduces the output power and specific power by 6%, but raises the system efficiency by 1%.

Table 4 shows that replacement of the PFF RTG with an RTPV generator having Boeing's measured filter and cell performance, even without the projected performance improvements, would roughly double the generator's BOM efficiency and specific power. The optimized design's EOM power output of 71 watts may not be high enough to meet JPL's goal of 63 watts when irradiation effects are taken into account, but could be raised from 71 to 76 watts by going to 40" fins, which would increase the system mass to 8.2 kg.

Table 4 further shows that replacement of the RTG with an RTPV having Boeing's projected filter and cell performance would roughly quadruple the generator's efficiency and triple its specific power. Moreover, it's BOM power output of 134 watts would result in an EOM output greatly in excess of JPL's 63-watt goal. This excess power capability would not be wasted, since it could be used for faster post-encounter data transmission to Earth, which would significantly reduce the mission's operating costs. Alternatively, the system mass could be reduced to 5.7 kg through use of smaller fins, which would still leave a BOM output of 103 watts.

PROGRAMMATIC CONCLUSIONS

In spite of the RTPV system's potential performance superiority, the PFF project at present is likely to select the existing RTG technology because its technical maturity is much greater than that of the TPV system. There have been some successful tests of gallium antimonide cells, with and without filters, but these used unoptimized cells made for the solar power program that did not reflect the full potential of the TPV converters.

Recently, Boeing conducted a preliminary scaled-down test for JPL's PFF project that endeavored to simulate the RTPV system [20]. While they reported encouraging results (13.3% measured efficiency at 1010°C), the test was hampered by constrained funding ($250K) and time limits (6 months). These limits did not permit construction and optimization of new cells and filters, and forced the use of components left over from previous programs. Those components were not only unoptimized, but the cells used came from different production batches that did not even match each other's performance, partly because of differences in contact metallization. Also, the anti-reflection coatings used were not optimized for the RTPV application. In addition, the number of available components was too small to cover more than a small fraction of the simulated heat source's surface area. Because of these limitations, the test results - while encouraging - were far from demonstrating the full potential of the RTPV system.

A concerted development effort could fairly quickly determine whether the above shortcomings could, in fact, be corrected and result in predicted BOM performance improvements. A prudent demonstration program should consist of a sequence of three steps, with each step initiated after successful demonstration of the preceding one. The first step would be a component development effort to determine whether Boeing's projected filter transmittance and cell reflectance, together with improved anti-reflection coatings and cell contacts, can in fact be realized. The second step would be to perform additional analyses and tests to confirm that radiation-induced degradation is of acceptable magnitude. If so, the third step would be construction of a full-scale prototypic converter array with an electrically heated Mo/W canister and a water-cooled housing, and tests to demonstrate that its BOM performance matches analytical predictions.

But even if that is successfully completed, could technology-readiness for a nine-year flight mission be demonstrated in time for the PFF program? Ordinarily, that is a very time-consuming process, because of the need for the lengthy life tests to demonstrate reliability and performance stability. However, there are several aspects of the RTPV design that may greatly reduce the need for lengthy tests:

- The heat source employs standard GPHS modules that have already been developed, safety-tested, life-tested, and successfully used in RTGs on previous flight programs. Therefore, the costly safety tests need not be repeated as long as the launch vehicle is no more severe than the previously used Shuttle and Titan-4.
- The GPHS modules are completely enclosed in a canister, to prevent access of sublimates and outgassing products to the PV cells.
- The canister is coated with tungsten to minimize sublimation. At 1100°C, tungsten sublimation is only 10^{-6} atomic monolayers in ten years.
- The filters employ gold, which is stable at the cold converter temperature. There is no need to develop exotic new materials with unknown degradation effects. The projected filter improvements require geometric rather than chemical modifications.
- The TPV cells and arrays are derivatives of solar system PV arrays and can benefit from fabrication methods developed for those systems over many years.
- The alpha particles emitted by the fuel are completely stopped by the canister. Neutron and gamma emission are orders of magnitude less than from reactors, and their effect on PV cells can be measured quickly by accelerated tests.
- Most important, the lengthy tests usually required to determine temperature-induced degradation effects are not needed, because RTPV cells operate cold (0-10°C).

The above factors may minimize the need for long-term testing and make it possible to establish the RTPV system's flight readiness within the required PFF schedule, if their development is initiated soon. In any event, it is clear that the very substantial improvements in system efficiency and specific power that would result from successful development of radioisotope thermophotovoltaic generators by DOE and/or NASA would make such systems of great value not only for the Pluto Fast Flyby mission but also for other missions requiring small, long-lived, low-mass generators in the future.

ACKNOWLEDGMENTS

The author takes pleasure in acknowledging the contributions of E. Horne and M. Morgan of the Boeing Company in providing the theoretical guidance and experimental data which formed the essential foundation of the present study. He also acknowledges the encouragement and support provided by A. Newhouse, Director of the Department of Energy's Space and Defense Power Systems Office, and of R. Lange, Director of its Radioisotope Power Systems Division; and appreciates the interest displayed by JPL's PFF Project Team led by R. Staehle.

REFERENCES

[1] Dochat, George R. and Dudenhoefer, James E., "Performance Results of the Stirling Power Converter" Proc. of the 11th Symposium on Space Nuclear Power Systems, CONF-940101, American Institute of Physics (AIP), New York, AIP Conference 301, 1994.

[2] Svedberg, Robert C., et al. "AMTEC Module Test Program," Proc. of the 11th Symposium on Space Nuclear Power Systems, CONF-940101, AIP Conference 301, 1994.

[3] Morgan, Mark D., W.E. Horne, and P.R. Brothers, "Radioisotope Thermophotovoltaic Power System Utilizing the GaSb IR Photovoltaic Cell," Proc. of the 10th Symposium on Space Nuclear Power Systems, CONF-930103, AIP Conference Proc. No 271, 1993.

[4] Fraas, L.M., G. Girard, J. Avery, B. Arau, V. Sundaram, A. Thompson, and J. Gee, "GaSb Booster Cells for over 30% Efficient Solar-Cell Stacks," J. Appl. Phys., 66 (8), 1989, 3866.

[5] Staehle, R., S. Weinstein, C. Salvo, and R. Terrile, "PLUTO Mission Progress Report: Lower Mass and Flight Time Through Advanced Technology," IAF-93-Q.5.410, 44th Congress of the International Astronautical Federation, Graz, Austria, 16-22 October 1993.

[6] Stern, Allen, "The Pluto Reconnaissance Flyby Mission," in Trans. of the American Geophysical Union, Vol. 74#7, February 16, 1993, p 73, 76-78.

[7] Jet Propulsion Laboratory, "Pluto Fast Flyby Program Environmental Impact Statement Supporting Study. Volume 2: Spacecraft Power Alternatives," JPL Publication No. D-10844, June 14, 1993.

[8] Schock, A., "RTG Options for Pluto Fast Flyby Mission," IAF-93-R.1.425a, 44th Congress of the International Astronautical Federation, Graz Austria, 16-22 October 1993.

[9] Schock, A., "RSG Options for Pluto Fast Flyby Mission," IAF-93-R.1.425b, 44th Congress of the International Astronautical Federation, Graz Austria, 16-22 October 1993.

[10] Schock, A., "Design Evolution and Verification of the General-Purpose Heat Source," #809203 in Proc. of 15th Intersociety Energy Conversion Engineering Conference, held in Seattle, WA, 1980.

[11] Schock, A., "Use of Modular Heat Source Stack in RTGs," #799305 in Proc. of 14th Intersociety Energy Conversion Engineering Conference, held in Boston, MA, 1979.

[12] Denham, H.B., et. al. "NASA Advanced Radiator C-C Thin Development," Proc. of the 11th Symposium on Space Nuclear Power Systems, CONF-940101, AIP Conference 301, 1994.

[13] Touloukian, Y.S. and D.P. Devitt, Thermophysical Properties of Matter, Vol 7; Thermal Radiative Properties, Metallic Elements and Alloys, 1970.

[14] Schock, A. and H. Sookiazian, "Design Optimization of RTG for Solar-Polar Mission," #799307 in Proc. of 14th Intersociety Energy Conversion Engineering Conference, held in Boston, MA, 1979.

[15] MSC/NASTRAN, Versions 65 thru 67.5. Based on NASA's NASTRAN general purpose structural analysis program. Developed and maintained by McNeal-Schwindler Corporation (MSC), CA.

[16] VibroAcoustic Payload Environment Prediction Systems (VAPEPS). Database maintained at the VAPEPS Management Center, JPL, Pasadena, CA.

[17] Miner, M.A., "Cumulative Damage in Fatigue," J. Appl. Mech., 12, September 1945.

[18] Gaski, J., SINDA (System Improved Numerical Differencing Analyzed), version 1.315 from Network Analysis Associate, Fountain Valley, CA, 1987.

[19] Little, A.D., SSPTA (Simplified Space Payload Thermal Analyzer), version 3.0/VAX, by Arthur D. Little Inc., for NASA/Goddard, by Arthur D. Little Inc., Cambridge, MA, 1986.

[20] Boeing Defense and Space Group, "Thermophotovoltaic Thermal-to-Electric Conversion Systems Report," Final Report to JPL on Contract 959595, December 20, 1993.